Surprisingly Robust Photochemistry in Subarctic Particles During Winter: Evidence from Photooxidants

Laura M. D. Heinlein[1], Junwei He[1], Michael Oluwatoyin Sunday[1*], Fangzhou Guo[2**], James Campbell[3], Allison Moon[4], Sukriti Kapur[5], Ting Fang[5***], Kasey Edwards[5], Meeta Cesler-Maloney[3****], Alyssa J. Burns[1], Jack Dibb[6], William Simpson[3], Manabu Shiraiwa[5], Becky Alexander[4], Jingqiu Mao[3], James H. Flynn III[2], Jochen Stutz[7], Cort Anastasio[1]

[1]Department of Land, Air and Water Resources, University of California, Davis, California 95616, USA
[2]Department of Earth & Atmospheric Sciences, University of Houston, Houston, TX 77204, USA
[3]Department of Chemistry and Biochemistry, University of Alaska, Fairbanks, Alaska 99775, USA
[4]Department of Atmospheric Sciences, University of Washington, Seattle, WA 98195, USA
[5]Department of Chemistry, University of California, Irvine, CA 92697, USA
[6]College of Engineering & Physical Sciences, University of New Hampshire, Durham, NH 03824, USA
[7]Department of Atmospheric & Oceanic Sciences, University of California, Los Angeles, CA 90095, USA

* Now at: California Air Resources Board, Sacramento, CA, USA
** Now at: Center for Atmospheric and Environmental Chemistry, Aerodyne Research Inc, Billerica, Massachusetts 01821, USA
*** Now at: Sustainable Energy and Environment Thrust, The Hong Kong University of Science and Technology (Guangzhou), Guangzhou, Guangdong 511400, China
**** Now at: Louisville Metro Air Pollution Control District, Louisville, Kentucky 40203, USA

Correspondence to: Cort Anastasio (canastasio@ucdavis.edu)

Abstract. Subarctic cities notoriously experience severe winter pollution episodes with $PM_{2.5}$ concentrations above 35 µg m^{-3}, the US EPA's 24-hour standard. While winter sources of primary particles in Fairbanks, Alaska have been studied, the chemistry driving secondary particle formation is elusive. Biomass burning is a major source of wintertime primary particles, making the $PM_{2.5}$ rich in light-absorbing brown carbon (BrC). When BrC absorbs sunlight, it produces photooxidants – reactive species potentially important for secondary sulfate and secondary organic aerosol formation – yet photooxidant measurements in high-latitude $PM_{2.5}$ remain scarce. During the winter 2022 ALPACA field campaign in Fairbanks, we collected PM filters, extracted the filters into water, and exposed the extracts to simulated sunlight to characterize the production of three photooxidants: oxidizing triplet excited states of BrC, singlet molecular oxygen, and hydroxyl radical. Next, we used our measurements to model photooxidant production in highly concentrated aerosol liquid water. While conventional wisdom indicates photochemistry is limited during high-latitude winters, we find that BrC photochemistry is significant: we predict high triplet and singlet oxygen daytime particle concentrations up to 2×10^{-12} M and 3×10^{-11} M, respectively, with moderate hydroxyl radical concentrations up to 5×10^{-15} M. Although our modeling predicts triplets account for 0.4-10% of daytime secondary sulfate formation, particle photochemistry cumulatively dominates, generating 76% of daytime secondary sulfate formation largely due to in-particle hydrogen peroxide, which contributes 25-54%.

Finally, we estimate triplet production rates year-round revealing highest rates in late winter when Fairbanks experiences severe pollution and in summer when wildfires generate BrC.

1 Introduction

In 2022, Fairbanks, Alaska, was ranked the third-worst US city for fine particle ($PM_{2.5}$) pollution, averaging 30 days per year above 35 µg m^{-3}, the US EPA's 24-hour standard (Simpson et al., 2024). Like Fairbanks, cities across the Arctic and subarctic suffer from severe winter $PM_{2.5}$ pollution episodes (Arnold et al., 2016; Schmale et al., 2018; Simpson et al., 2024). These pollution events are caused by local emissions and unfavorable meteorology, where strong surface-based inversions trap locally emitted pollution in the bottom 20 meters of the atmosphere (Cesler-Maloney et al., 2022; Simpson et al., 2024). While the meteorology driving pollution episodes has been characterized (Brett et al., 2024; Cesler-Maloney et al., 2024), and many of the primary sources of PM have been identified, the secondary chemical processes that form and transform PM in Fairbanks are only starting to be explored (Moon et al., 2024; Simpson et al., 2024; Sunday et al., 2025). These secondary processes can produce PM, worsening air quality, and need to be characterized for a complete understanding of PM pollution in Fairbanks (Ijaz et al., 2024; Joo et al., 2024; Mao et al., 2024; Moon et al., 2024; Sunday et al., 2025; Virtanen et al., 2010).

Winter $PM_{2.5}$ in Fairbanks is, on average, 60% organic aerosol (OA), 20% sulfate (SO_4^{2-}), with the remaining 20% a combination of elemental carbon, nitrate, ammonium, and other inorganic ions (Kotchenruther, 2016; Robinson et al., 2024; Simpson et al., 2024). The dominant sources of primary $PM_{2.5}$ – fine particles emitted directly into the atmosphere – are residential wood burning, combustion of sulfur-rich fuel oil, and vehicle emissions (Moon et al., 2024; Robinson et al., 2023; Simpson et al., 2024). Secondary $PM_{2.5}$ formation – the oxidation of gases to form low volatility products – has also been identified as a PM source in Fairbanks (Ijaz et al., 2024; Moon et al., 2024; Robinson et al., 2024; Simpson et al., 2019). Kotchenruther et al. (2016) reported that in Fairbanks winters, on average 12% of OA is secondary (i.e., SOA) or aged woodsmoke OA – both formed by secondary chemistry. Similarly, during the Alaskan Layered Pollution And Chemical Analysis (ALPACA) field campaign in 2022, between 16 and 58% of total SO_4^{2-} was secondary (Moon et al., 2024). While it is evident that secondary PM comprises a substantial portion of winter $PM_{2.5}$ in Fairbanks, the oxidants driving this observed secondary PM formation remain unclear (Simpson et al., 2019).

In Fairbanks, the abundance of biomass burning PM indicates a strong potential for condensed-phase brown carbon (BrC) photochemistry. Biomass burning (BB) particles are rich in BrC – light-absorbing organic compounds formed during the incomplete combustion of biomass, as well as fossil fuel combustion and multiphase chemical processing (Laskin et al., 2025). When BrC chromophores absorb light, they form photooxidants – reactive species that can produce secondary sulfate and secondary organic aerosol (Jiang et al., 2021; Sunday et al., 2025; Wang et al., 2020b). We focus on three photooxidants that are important for condensed-phase reactions in woodsmoke particles: hydroxyl radical ($^{\bullet}OH$), oxidizing triplet excited states of BrC ($^3C^*$ or "triplets"), and singlet molecular oxygen ($^1O_2^*$) (Bogler et al., 2022; Chen et al., 2018; Kaur et al., 2019; Kaur and Anastasio, 2018; Lyu et al., 2023; Ma et al., 2023, 2024; Manfrin et al., 2019). As shown in Figure 1, these photooxidants, which are formed by sunlight reactions involving brown carbon, can be significant intermediates in the formation of secondary PM species.

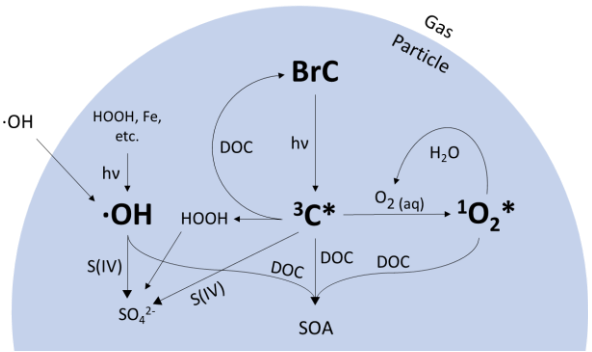

Figure 1. Schematic of condensed-phase •OH, $^3C^*$, and $^1O_2^*$ formation from brown carbon (BrC) photochemistry.

Hydroxyl radicals in aqueous droplets can be formed through a variety of mechanisms. In cloud/fog water, where the PM-mass/H_2O-mass ratio is between 10^{-3} and 10^{-4} (Ma et al., 2023), transport of •OH from the gas phase is an important source of aqueous-phase •OH. In aerosol liquid water (ALW), where the PM-mass/H_2O-mass ratio is close to 1 (Ma et al., 2023), in situ photochemical production of •OH becomes the dominant source (Kaur et al., 2019; Ma et al., 2023). Aqueous-phase •OH can be produced by reactions of hydrogen peroxide with reduced iron or copper, the decomposition and photolysis of organic hydroperoxides, the photolysis of nitrate and nitrite, and as a byproduct of BrC photochemistry (Arciva et al., 2022; Gerritz et al., 2023, 2024; Tomaz et al., 2018; Tong et al., 2016). In addition, Kapur et al. (2024) report production of •OH in dark samples from the ALPACA campaign using EPR. The dominant sink for photochemical •OH in cloud water and ALW is dissolved organic carbon (DOC) (Arakaki et al., 2013): hydroxyl radicals react rapidly with organic compounds and can form aqueous secondary organic aerosol, which may contribute to the abundant OA observed in Fairbanks (Arciva et al., 2022; Smith et al., 2015; Yu et al., 2014). Aqueous-phase •OH also reacts with S(IV) to form secondary SO_4^{2-}, which may contribute to the sulfate observed in Fairbanks (Seinfeld and Pandis, 2016).

Oxidizing triplet excited states of brown carbon are formed when BrC chromophores absorb sunlight, forming an electronically excited state chromophore (Kaur and Anastasio, 2018; McNeill and Canonica, 2016). $^3C^*$ concentrations in the atmosphere were first measured in cloud and fog drops, but recent work showed much higher levels in ALW (Kaur and Anastasio, 2018; Ma et al., 2023). These results suggest that triplets are kinetically competitive against other particle oxidants like •OH and indicate the strong potential for $^3C^*$-driven chemistry in particles (Ma et al., 2023). Specifically, triplets might be an important oxidant in secondary SO_4^{2-} formation in BrC-rich aerosols due to in situ particle chemistry and surface reactions (Wang et al., 2020b; Liang et al., 2024). They can also rapidly convert phenols to aqueous SOA in drops and particles (Jiang et al., 2023b, a; Ma et al., 2021, 2024; Smith et al., 2014, 2016; Yu et al., 2014; Zhang et al., 2022), and form secondary oxidants such as phenoxy radicals which may drive additional chemistry (Remke et al., 2022).

The third photooxidant of interest in BrC-rich particles is singlet molecular oxygen, which is produced when triplets transfer their energy to dissolved oxygen (Figure 1; Appiani and McNeill, 2015). Of the three photooxidants discussed here, $^1O_2*$ is predicted to exhibit the highest steady-state concentrations in ALW, roughly 10 times higher than that of triplets and 100-1000 times higher than aqueous $^\bullet OH$ (Kaur et al., 2019; Ma et al., 2023). Interestingly, the concentration of $^1O_2*$ is highly dependent on the type of BrC and varies greatly among BrC sources (Jiang et al., 2023a; Ma et al., 2024; Manfrin et al., 2019). While $^1O_2*$ concentrations in ALW are higher than those of $^3C*$ and $^\bullet OH$ in ALW, singlet oxygen is also more selective: $^1O_2*$ reacts with fewer organic species and with slower reaction rates than $^3C*$ and $^\bullet OH$ (Manfrin et al., 2019). Nonetheless, in ALW, singlet oxygen can be a significant sink for some organic species and might also be important for aqueous SOA formation (Ma et al., 2023; Manfrin et al., 2019).

Given the potential importance of photooxidants and the lack of measurements, our goal is to quantify photooxidant production in wintertime particles from a high-latitude site to understand their role in the multiphase chemical processing during severe winter pollution events. First, we measure the photolytic production of aqueous-phase $^\bullet OH$, $^3C*$, and $^1O_2*$ in dilute extracts of $PM_{2.5}$ collected in Fairbanks during ALPACA. We then use these extract measurements to model photooxidant production in aerosol liquid water to understand wintertime photooxidant production in biomass burning PM. To explore how $^3C*$ and other oxidants contribute to chemical processing in particles, we first assess the lifetimes of various organic species due to $^\bullet OH$, $^3C*$, and $^1O_2*$. We next build a kinetic model to estimate the importance of triplet excited states and other oxidants in the formation of secondary sulfate. Lastly, we predict $^3C*$ production in particles throughout the year in Fairbanks to assess the overall potential for $^3C*$ chemistry.

2 Methods

2.1 Chemicals

Syringol (SYR, 99%), furfuryl alcohol (FFA, 98%), benzoic acid (BA, ≥ 99.5%), *p*-hydroxybenzoic acid (*p*-HBA, 99%), 3,4-dimethoxybenzaldehyde (DMB, 99%), and methanol (MeOH, ≥ 99.5%) were received from Millipore Sigma. Chemical solutions and particulate matter extracts (PME) were prepared using air-saturated ultrapure water (Milli-Q water) from a Milli-Q Advantage A10 system (Millipore; ≥18.2 MΩ cm) that was pretreated with a Barnstead activated carbon cartridge. pH was adjusted with TraceMetal™ Grade concentrated sulfuric acid (Fisher Scientific, 18.4 M).

2.2 Sample Collection, Extraction, and Storage

Between January 13th and February 25th, 2022, high-volume 24-hour filter samples of ambient particles were collected at two separate sites in Fairbanks: a residential location designated as the "House" site, and at the University of Alaska Fairbanks Community & Technical College in downtown Fairbanks called the "CTC" site (Simpson et al., 2024). We collected $PM_{2.5}$ at the House site and $PM_{0.7}$ (particulate matter ≤ 2.5 and ≤ 0.7 µm in diameter, respectively) at the CTC site. Details regarding filter collection at the house and CTC sites are outlined in Edwards et al. (2024) and Moon et al. (2024), respectively, and in Section S1. While we measured photooxidants on all House site composites, we only performed a few measurements of photooxidants using the CTC composites, and instead used them to perform the dilution series experiment (outlined below), to explore site differences, and to examine pH differences.

The 24-hour filters were compiled into multiday composites, with each composite named with its midpoint date (Table S1, Figure 2). To prepare PME, filters were first cut into 2×2 cm squares (with several squares cut from each filter), placed in individual 20 mL amber bottles, and submerged in 1.0 mL of solvent. For a given composite, we used an equal number of filter squares from each filter to ensure that each day was equally represented. In other words, we controlled the ratio of filter area from each individual filter to the total area of filter extracted to create a composite. Filters were extracted either in Milli-Q water, 50 mM sulfuric acid (pH 1.3, henceforth referred to as pH 1), or 10 µM sulfuric acid (pH 4.7, henceforth referred to as pH 5). House site filters were extracted into only Milli-Q water and pH 1, while some CTC site filters were extracted into pH 5 in addition to Milli-Q water and pH 1. The two concentrations of sulfuric acid were selected to mimic the high and low pH values predicted in aerosol liquid water by Campbell et al. (2024). The filters in solution were shaken for four hours in the dark, after which the filter squares were removed and extracts in a given solvent were combined. For each filter, we made up 2-3 different extracts: Milli-Q, pH 1, and for some filters, pH 5. The extracts were filtered (0.22 µm PTFE; Pall), their pH values were measured (Table S2), and for pH 5 extracts, which generally had an initial pH above 5, additional sulfuric acid was added to adjust to within 0.2 pH units of pH 5. The solutions were then flash-frozen in liquid nitrogen and stored in a -20 ºC freezer until further use. The pH 1 and pH 5 particle extracts were used to measure photooxidant production, UV-Vis absorbance spectra, and concentrations of water-soluble transition metals, while parallel Milli-Q extracts were used to determine concentrations of total solutes, DOC, and ions.

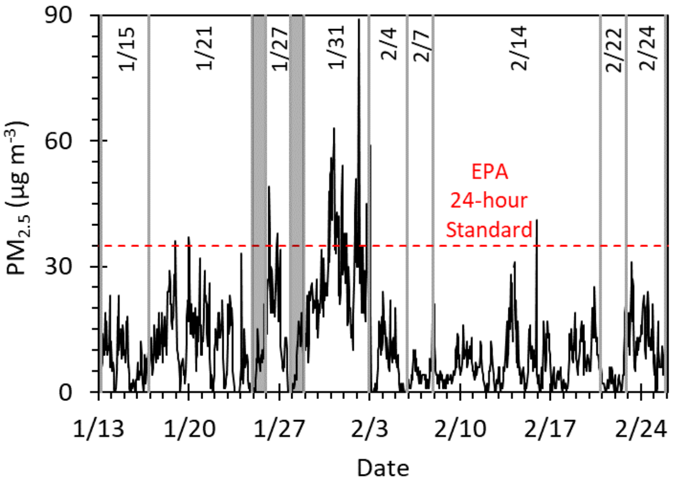

Figure 2. Hourly average PM$_{2.5}$ mass concentrations in downtown Fairbanks (NCore site; Simpson et al., 2024) for the ALPACA campaign of winter 2022. Grey lines delineate each composite, labelled with its midpoint date, while grey-shaded days were used for initial testing and were not part of a composite (see Table S1 for collection times). The red dashed line marks the EPA 24-hour PM$_{2.5}$ standard.

2.3 General Sample Composition

The UV-Vis absorbance spectrum of each composite was measured with a Shimadzu UV-2501PC spectrophotometer in a 1-cm quartz cuvette. The pH of each extract from every composite was measured using a microelectrode (MI-414 series, protected tip; Microelectrodes, Inc.) The DOC concentration of each composite was measured using a Shimadzu Total Organic Carbon Analyzer (TOC-V CSH). Dissolved metal concentrations of each composite were measured using an Agilent Technologies triple-quadrupole 8900 Inductively Coupled Plasma Mass Spectrometer. The concentrations of major ions of each composite using ion chromatography (Dionex ICS-6000) (Sunday et al., 2025).

2.4 Illumination Experiments

Illumination experiments were performed as outlined in Ma et al. (2024) and briefly reviewed here. Tropospheric sunlight was simulated with a 1000 W xenon arc lamp with three downstream optical filters: a water filter, an AM1.0 air mass filter (AM1D-3L, Sciencetech), and a 295 nm long-pass filter (20CGA-295, Thorlabs; see Figure S1 for the simulated sunlight spectrum; (Kaur and Anastasio, 2018; Ma et al., 2023; Sunday et al., 2025). All illuminations were performed in 1 mL GE 021 quartz tubes (5 mm inner diameter). On each experiment day, the photolysis rate constant of 10 µM of 2-nitrobenzaldehyde ($j_{2NB,EXP}$) was measured and used to determine the daily photon flux in the solar simulator (Galbavy et al., 2010). Values of $j_{2NB,EXP}$ ranged from 0.018 to 0.026 s^{-1} (decay plots are shown in Figure S2); all laboratory oxidant production rates and concentrations reported in this work were normalized to a standard $j_{2NB,AK}$ of 0.0045 s^{-1}, a value representative of the Fairbanks midday actinic flux on February 1st, 2022 using actinic sunlight modeled by Tropospheric Ultraviolet and Visible (TUV) Radiation (Madronich and Flocke, 1998). This $j_{2NB,AK}$ value also includes an enhancement factor of 2.5 to account for optical confinement (described in Section 3.1) (Corral Arroyo et al., 2022). Light screening, i.e., the attenuation of photons through the reaction tube, was quantified using a screening factor (S_λ) (Section S2). The rate of light absorbance by PM extracts in the solar simulator was calculated as described in Section S3.

2.5 Photooxidant Measurements

Steady-state concentrations of $^\bullet$OH, $^3C^*$, and $^1O_2^*$ were measured under laboratory conditions with widely used probe methods (Anastasio and McGregor, 2001; Appiani et al., 2017; Appiani and McNeill, 2015; Kaur et al., 2019; Kaur and Anastasio, 2018; Ma et al., 2022). Benzoic acid, syringol, and furfuryl alcohol were used to measure $^\bullet$OH, oxidizing $^3C^*$, and $^1O_2^*$, respectively, by quantifying the loss of the probes during illumination. For benzoic acid, we also monitored the formation of a product, *p*-HBA (Section S4). For each experiment, 1.0 mL of particulate matter extract was spiked with 10 µM of a probe (*P*), held at 10 °C, and illuminated. Solutions were not stirred since the entire solution was illuminated, but solutions were shaken vigorously prior to illumination and sampling to ensure homogeneity. At five designated timepoints, a 130 µL aliquot was removed and the probe concentration was determined using high pressure liquid chromatography (HPLC: Shimadzu LC-20AB pump, Thermo Scientific Accucore XL C18 column (50 × 3 mm, 4 µm bead), and Shimadzu-M20A Photodiode Array detector). The probe decay was then fit with the first-order kinetic equation:

$$ln\frac{[P_\mathrm{t}]}{[P_0]} = -k'_\mathrm{P}\ t \qquad (1)$$

where *t* is time, $[P_\mathrm{t}]$ was the probe concentration at time *t*, $[P_0]$ was the initial probe concentration, and k'_P was the measured pseudo-first order rate constant for probe loss (raw data are shown in Figure S2). The k'_P was then corrected for internal light screening and normalized to a $j_{2NB,AK}$ of 0.0045 s^{-1} using

$$k'_\mathrm{P,EXP} = \frac{k'_\mathrm{P}\ 0.0045}{S_\lambda\ j_\mathrm{2NB,EXP}} \qquad (2)$$

where $k'_\mathrm{P,EXP}$ was the normalized pseudo-first order rate constant for *P* loss and S_λ was the screening factor. Parallel dark control experiments were performed by measuring probe concentrations in a quartz tube containing the particulate matter extract spiked with all three probes and wrapped in aluminum foil. No probe loss was observed in the dark samples. Using the experimental k'_P, the steady-state oxidant concentrations and oxidant production rates were calculated using methods described in Sections S4 and S5 and rate constants from Table S3. Finally, the quantum yield (Φ_Ox) of each oxidant in our dilute extracts was determined by

$$\Phi_{\mathrm{Ox}} = \frac{P_{\mathrm{Ox,EXP,PME}}}{R_{\mathrm{abs,EXP,PME}}} \tag{3}$$

where $P_{\mathrm{Ox,EXP,PME}}$ is the production rate of a given oxidant and $R_{\mathrm{abs,EXP,PME}}$ is the rate of light absorbance of our PME (Section S3), both under laboratory experimental conditions with a standard photon flux of $j_{\mathrm{2NB,AK}} = 0.0045\ \mathrm{s}^{-1}$.

2.6 Predicting Photooxidant Concentrations in Aerosol Liquid Water of Fairbanks Particles

2.6.1 Sunlight in Fairbanks

Throughout ALPACA, the downwelling spectral actinic flux (310-700 nm) was measured every 8 minutes using a diode array actinic flux spectroradiometer (MetCon Gmbh) at the NCore site in downtown Fairbanks (calibrated prior to the ALPACA campaign). To quantify albedo, upwelling and downwelling j_{NO2} values were measured at one-minute intervals using a filter radiometer (MetCon Gmbh, calibrated after the ALPACA campaign). The upwelling-to-downwelling ratio of j_{NO2} was calculated and applied to the downwelling spectral actinic flux to estimate the total (i.e., upwelling and downwelling) actinic flux. Using this data, we calculated the daily peak three-hour average actinic flux ($I_{\lambda,\mathrm{AK}}$). We then averaged the daily peak three-hour $I_{\lambda,\mathrm{AK}}$ over each composite to calculate an $I_{\lambda,\mathrm{AK}}$ representative of the peak-three hour average sunlight condition for each composite. The rate of light absorbance ($R_{\mathrm{abs,AK,ALW}}$, mol $\mathrm{L}^{-1}\ \mathrm{s}^{-1}$) of BrC in Fairbanks particles was then calculated with

$$R_{\mathrm{abs,AK,ALW}} = [\mathrm{DOC}]_{\mathrm{ALW}} \times \sum_{310}^{550} [\mathrm{MAC}_{\lambda} \times I_{\lambda,\mathrm{AK}} \times \Delta\lambda \times 10^{-3}] \times (a+1) \times 2.5 \tag{4}$$

where $[\mathrm{DOC}]_{\mathrm{ALW}}$ was the water-soluble DOC concentration predicted for ALW conditions (mg L^{-1}), MAC_{λ} was the DOC-normalized mass absorption cross section at wavelength λ ($\mathrm{cm}^2\ \mathrm{g}^{-1}$), $I_{\lambda,\mathrm{AK}}$ was the composite-average peak three-hour actinic flux based on measurements during ALPACA (mol-photons $\mathrm{cm}^{-2}\ \mathrm{nm}^{-1}\ \mathrm{s}^{-1}$), Δλ was the wavelength interval between discreet $I_{\lambda,\mathrm{AK}}$ values (1 nm), the 10^{-3} factor was a unit conversion of g to mg, a was the albedo, and 2.5 was a factor that accounted for optical confinement (Corral Arroyo et al., 2022; Kaur et al., 2019). We defined our ALW conditions based on the ALW concentrations reported by Campbell et al. (2024) modelled using ISORROPIA-II during the ALPACA campaign. DOC concentrations in ALW were calculated as described in Section S6.

2.6.2 Dilution Series

To predict the steady-state concentrations of $^{\bullet}\mathrm{OH}$, $^3\mathrm{C}^*$, and $^1\mathrm{O}_2^*$ in aerosol liquid water in Fairbanks, we first characterized how oxidant concentrations changed with solution concentration (Kaur et al., 2019; Ma et al., 2023). We performed a dilution experiment on the 2/14 CTC composite. We prepared five separate particulate matter extracts, extracting the 2×2 cm filter squares into different volumes of solution to obtain a sequence of dilutions (prepared in pH 1, with parallel Milli-Q extracts prepared for the three most dilute samples). Compared to standard particulate matter extract, where a 2×2 cm filter square was extracted into 1.0 mL of solution, the five dilution series extracts were prepared with solution volumes equal to extracting each 2×2 cm filter squares into 10.0, 2.0, 0.70, 0.40, and 0.30 mL of solution. For the three most dilute extracts, we extracted the filters into 50 mM H_2SO_4 (pH 1.3). For the 0.40 mL-per-square and 0.30 mL-per-square extractions, we extracted the filter squares into 1.0 mL of 0.020 M and 0.015 M H_2SO_4, respectively. We then used rotary evaporation to concentrate the extracts (removing 60% and 70% of the water for the 0.40 mL and 0.30 mL samples, respectively), a technique described and validated by Ma et al. (2024). The final extracts had H_2SO_4 concentrations of roughly 50 mM, which was verified with pH measurements (i.e., pH 1.3). We then measured the $^{\bullet}$OH, ^{3}C*, and $^1O_2$* concentrations in each of the five extracts to understand how photooxidant concentrations change as a function of extract concentration. We also measured DOC in all five extracts (in Milli-Q extracts of the 3 most dilute samples and in pH 1 PME for the 2 concentrated samples) and measured water-soluble metals and ions in the Milli-Q extracts of the three most dilute samples to validate that DOC, ions, and metals all changed linearly with the dilution (Sunday et al., 2025); there was insufficient sample volume to measure metals and ions in the two most concentrated samples.

2.6.3 Modelling Photooxidant Production in Aerosol Liquid Water

We extrapolated steady-state concentrations of $^{\bullet}$OH, ^{3}C*, and $^1O_2$* in aerosol liquid water from our particle extract results using the kinetic models developed by Ma et al. (2024) and Kaur et al. (2019). The model was based on the definition of steady-state concentration:

$$[\mathrm{Ox}] = \frac{P_{\mathrm{Ox}}}{k'_{\mathrm{Ox}}} \tag{5}$$

where the oxidant concentration ([Ox]) was equal to the ratio of the production rate (P_{Ox}) to the pseudo-first-order rate constant for oxidant loss (k'_{Ox}). We used DOC concentration as a proxy for aerosol liquid water content (ALWC), with higher DOC concentrations corresponding to lower ALWC (Ma et al., 2023). For the dilution series composite, we calculated P_{Ox}, k'_{Ox}, and oxidant concentrations at a wide range of liquid water content, from fog/cloud drops to particle water; for all other composites, we only determined these values under ALW conditions.

We modeled the steady-state $^{\bullet}$OH concentration in ALW by calculating both the $^{\bullet}$OH production rate ($P_{\bullet\mathrm{OH,ALW}}$) and the major $^{\bullet}$OH sink ($k'_{\bullet\mathrm{OH,ALW}}$). Laboratory experiments determined that $P_{\bullet\mathrm{OH,PME}}$ is proportional to DOC (Kaur et al., 2019; Ma et al., 2023), which we verified for our samples in the dilution series experiment. As such, we assumed the quantum yield determined in the dilute particle extracts under laboratory simulated sunlight, $\Phi_{\bullet\mathrm{OH}}$ was constant across cloud/fog and ALW conditions. $P_{\bullet\mathrm{OH,ALW}}$ was calculated with

$$P_{\bullet\mathrm{OH,ALW}} = \Phi_{\bullet\mathrm{OH}} \times R_{\mathrm{abs,AK,ALW}} \tag{6}$$

where $R_{\text{abs,AK,ALW}}$ was the rate of light absorbance in ALW conditions under Fairbanks sunlight. We estimate the contribution of $^{\bullet}$OH in particles from gas-phase $^{\bullet}$OH mass transport using the Fuchs-Sutugin transition regime theory (Seinfeld & Pandis, 2016; Tables S4, S5, S6). The total aqueous-phase $P_{\bullet\text{OH,ALW}}$ was the combined rate of photochemical $^{\bullet}$OH formation inside particles and uptake rate of $^{\bullet}$OH from the gas phase. We calculate the sink for $^{\bullet}$OH considering only reactions with DOC ($k_{\text{DOC+}\bullet\text{OH}} = 3.8(\pm1.9)\times10^{8}$ L mol-C^{-1} s^{-1}; Arakaki et al., 2013) since this was the dominant loss for $^{\bullet}$OH under dilute and ALW conditions (Arakaki et al., 2013; Kaur et al., 2019; Ma et al., 2023). Once $P_{\text{Ox,ALW}}$ and $k'_{\text{Ox,ALW}}$ were determined, the $^{\bullet}$OH concentration was calculated using equation 5.

Similar to $P_{\bullet\text{OH,PME}}$, laboratory experiments have shown that $P_{3\text{C}*,\text{PME}}$ is also proportional to solute concentration, which we tested with our dilution series samples (Kaur et al., 2019; Ma et al., 2023). $P_{3\text{C}*,\text{ALW}}$ was calculated with an equation analogous to equation 6, instead using $\Phi_{3\text{C}*}$. The rate constant for triplet loss in ALW ($k'_{3\text{C}*,\text{ALW}}$) was estimated by considering three sinks for triplets: energy transfer to dissolved O_2, chemical reaction with DOC, and physical quenching by DOC (Ma et al., 2024). The average second-order rate constant for the reaction of ^{3}C* with O_2 ($k_{\text{O2+3C}*}$) was estimated by Kaur et al. (2019) as 2.8×10^{9} M^{-1} s^{-1}. The concentration of O_2 in Fairbanks particle water was estimated using the temperature-dependent Henry's Law constant and composite-averaged temperature measurements, assuming negligible influence of ionic strength (Seinfeld and Pandis, 2016). The second-order rate constant for reaction and quenching of oxidizing ^{3}C* with DOC ($k_{\text{rxn+Q,3C}*,\text{SYR}}$) measured in biomass-burning PM extracts with the syringol (SYR) probe was 7×10^{7} M^{-1} s^{-1} (Ma et al., 2024). Once $k'_{3\text{C}*,\text{ALW}}$ was calculated, the ^{3}C* concentration was predicted using equation 5.

While $P_{1\text{O2}*,\text{PME}}$ increased linearly with DOC concentration in PM extracts, which are dilute, Ma et al. (2023) have shown that the production rate plateaus at the high DOC concentrations of ALW. We captured this behavior in $P_{1\text{O2}*}$ across both PME and ALW conditions using the formulation from Ma et al. (2023):

$$P_{1O2*} = \frac{\frac{\Delta P_{1\text{O2}*}}{\Delta\text{DOC}} \times [\text{DOC}]}{1 + \left(\frac{k_{\text{rxn+Q,3C}*,\text{FFA}}[\text{DOC}]}{k_{\text{O2+3C}*}\,[\text{O}_2]}\right)} \qquad (7)$$

where $\frac{\Delta P_{1\text{O2}*}}{\Delta\text{DOC}}$ was the ratio of $^{1}O_2$* production rate to DOC concentration for a given sample in dilute solutions and $k_{\text{rxn+Q,3C}*,\text{FFA}}$ was the second-order rate constant for reaction and quenching of the entire pool of ^{3}C* by DOC as measured with furfuryl alcohol (FFA) (1×10^{7} M^{-1} s^{-1}; Ma et al., 2024). We then calculated the pseudo-first-order rate constant for $^{1}O_2$* loss by using two $^{1}O_2$* sinks: quenching by water ($k'_{1\text{O2}*,\text{H2O}} = 2.76(\pm0.02)\times10^{5}$ s^{-1}, Appiani et al., 2017) and reaction with DOC ($k_{1\text{O2}*+\text{DOC}} = 1\times10^{5}$ M^{-1} s^{-1}, Ma et al., 2023). The $^{1}O_2$* concentration was then predicted using equation 5.

3 Results and Discussion

To assess the role of brown-carbon-mediated photochemistry during winter in Fairbanks, Alaska, we measured photooxidant production in nine composites of $PM_{2.5}$ filter samples collected at the House and CTC sites during the six-week ALPACA field campaign (Figure 2, Table S1). During the campaign, the composite average temperature at the CTC site ranged from -31 to -5 ºC and the composite average relative humidity ranged from 75 to 90% (Table S7; relative humidity was measured by the AK Department of Transportation < 1 mile from the CTC site). The most polluted period during the ALPACA campaign is captured by the 1/31 composite (1/29 to 2/3), with a peak hourly average $PM_{2.5}$ of 89 µg m^{-3} and a composite-average $PM_{2.5}$ concentration of 27 µg m^{-3} (Figure 2). The pollution episode exhibited low temperatures and high relative humidity, with a composite-average temperature of -31 °C and relative humidity of 75%. Details of each sample composite, including the sample collection time-period, average $PM_{2.5}$ concentration, ambient temperature, relative humidity, albedo, and peak three-hour composite-averaged actinic flux are listed in Table S7.

3.1 Is Condensed-Phase Photochemistry Possible in the Winter in Fairbanks?

Conventional wisdom holds that photochemical oxidant generation, such as $^{\bullet}OH$ formation from ozone photolysis, is slow and generally unimportant in high latitudes during winter. We sought to assess this for brown carbon photochemistry by examining whether BrC might be a significant source of winter oxidants in Fairbanks particles. Figure 3a compares the absorption cross sections of gas-phase O_3 and HONO and particulate BrC from the 1/31 House sample. Ozone absorbs very little wintertime sunlight, confirming its lack of photochemical activity during ALPACA. However, both HONO and BrC absorb significantly at longer wavelengths, suggesting they are likely sources of wintertime oxidants.

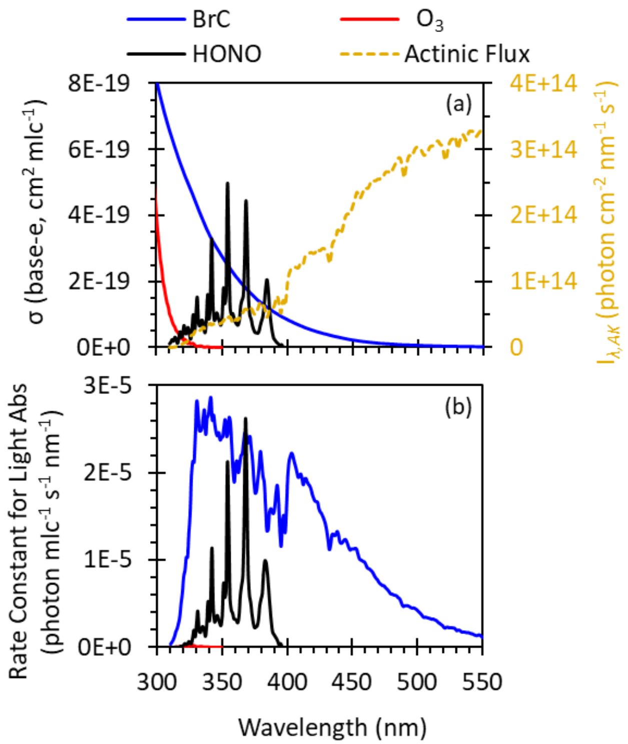

Figure 3. (a) Base-e absorption coefficients for particulate BrC (1/31 composite, expressed in units of per-carbon-atom of DOC), as well as gas-phase O_3 and HONO (Finlayson-Pitts and Pitts, 2000), overlaid with the measured total photon flux ($I_{\lambda,AK}$) at solar noon for the 1/31 polluted period. (b) Rate constant of light absorption of BrC (per-carbon-atom), O_3 (per-molecule), and HONO (per-molecule). The ozone result is indistinguishable from the x-axis. The brown carbon result includes a factor of 2.5 enhancement of $I_{\lambda,AK}$ due to optical confinement within particles (Section 3.1).

Figure 3b compares the per-molecule (or for BrC, per-carbon-atom) light absorbance rates of BrC, O_3, and HONO. Three factors enhance BrC photochemistry in Fairbanks' low sunlight environment. First, BrC significantly absorbs visible light ($\lambda > 400$ nm), while O_3 and HONO do not. Moreover, BrC and HONO both have significant UV-A absorbance and therefore are less impacted by the suppression of UV-B photons in winter sunlight, which limits O_3 photolysis (Seinfeld and Pandis, 2016). Second, Corral Arroyo et al. (2022) report a two- to three-fold enhancement of the photon flux inside particles due to optical confinement, which impacts particle-phase BrC but not gas-phase HONO or O_3 (the 2.5 factor is included in Figure 3b and in all ALW calculations) (Corral Arroyo et al., 2022). Third, sunlight during the winter in Fairbanks is enhanced by albedo: the composite average (±1σ) measured upwelling-to-downwelling ratio during the peak three hours of daylight was 0.85(±0.07) (Table S7), affecting all photochemistry. BrC absorbs 8 times more light than HONO and 1000 times more light than O_3 on a per-molecule (or per-carbon-atom) basis (Figure 3b), demonstrating the strong potential for BrC-mediated photochemistry.

3.1.1 Subarctic Winter Sunlight

Next, we explore how the intensity of sunlight changes throughout the campaign. Figure 4a compares the actinic flux at solar noon measured during ALPACA to predictions by the Tropospheric Ultraviolet and Visible (TUV) Radiation Model run with standard clear-sky conditions (Madronich and Flocke, 1998; TUV parameters in Table S8). The ratio of measured-to-modelled actinic flux ranged from 0.31 to 1.28, with an average (±1σ) of 0.62(±0.33). For periods when TUV underestimates the measurements, the error is likely because the 0.85 albedo used in our TUV input underestimates the midday albedo, which was often close to 1. For periods where TUV overestimates the measurements, we attribute this to cloudiness not accounted for in our TUV inputs. This is in line with the 50-70% reduction in actinic flux observed below clouds in previous work (Crawford et al., 2003). The most significant difference between measured and TUV-modeled actinic fluxes is at short wavelengths, where the model overpredicts (Figure S3). This is important for species like O_3 that absorb solely at short wavelengths but it has less of an impact on species such as BrC, which absorb strongly into the visible region (Figure 3).

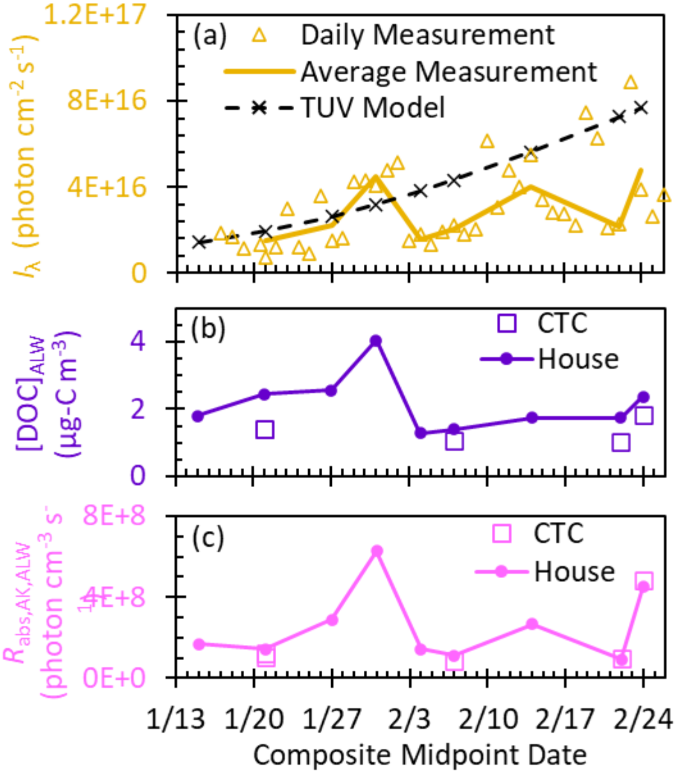

Figure 4. (a) Daily measured total (upwelling and downwelling) actinic flux ($I_{\lambda,\mathrm{AK}}$) summed from 310 to 550 nm measured at solar noon (gold triangles) and the corresponding midday values averaged for each composite (gold line). TUV modeled $I_{\lambda,\mathrm{AK}}$ summed from 310 to 550 nm at solar noon at the midpoint day of each composite (dashed black line), using an albedo of 0.85. All $I_{\lambda,\mathrm{AK}}$ values here are for the gas phase and are not affected by in-particle enhancement from optical confinement. (b) Dissolved organic carbon concentrations calculated in ALW (Section S6) at the two sampling locations (House and CTC). (c) Rate of light absorbance by DOC per volume of ALW using the measured three-hour midday $I_{\lambda,\mathrm{AK}}$ average for each composite. For the 1/15 composite, $I_{\lambda,\mathrm{AK}}$ was not measured and so the modelled $I_{\lambda,\mathrm{AK}}$ was used. $R_{\mathrm{abs,AK,ALW}}$ values account for the factor of 2.5 enhancement due to optical confinement in particles.

3.1.2 Light-Absorbing Properties of BrC

The composite-average DOC (Section S6) at the House site peaked during the 1/31 pollution event at 4 µg-C m^{-3} and averaged (±1σ) 2.2(±0.8) µg-C m^{-3} across the campaign (Figure 4b). In our samples, the average (±1σ) mass absorption coefficient at 300 nm (MAC_{300}) is 3.3(±0.8) m^2 $g\text{-}C^{-1}$ and the average (±1σ) Absorption Ångström Exponent (AAE, 300-450 nm) is 9.4(±0.6) (Figure S4 and Table S9). For the composites where we measured the MAC at both the House and CTC sites, we see only minor differences between the two sites (Table S9). While MAC_{300} is consistent throughout the campaign, MAC_{365} decreases ($p < 0.05$) suggesting photobleaching becomes more important as daylight hours increase (Laskin et al., 2015). Our MAC and AAE values are very similar to other urban polluted regions where residential wood burning is abundant (Li et al., 2020), and are slightly higher than values reported for wildfire-dominated samples (Bali et al., 2024; Jiang et al., 2023a; Ma et al., 2023). Since the MAC values of BrC from gasoline exhaust are a factor of two lower than those of woodsmoke BrC, our data suggest gasoline vehicles are not a dominant source of BrC during ALPACA (Xie et al., 2017). We also characterized our BrC with E2/E3, i.e., the ratio of absorbance at 250 nm to that at 365 nm (Helms et al., 2008; Peuravuori and Pihlaja, 1997). While E2/E3 values in aqueous $PM_{2.5}$ extracts have been reported between 4.2 and 17 (Ma et al., 2024), our sample values inhabit a small range, from 5.8 to 8. Low E2/E3 values correspond to high molecular weight compounds, indicating their ubiquity in our samples (Helms et al., 2008; Ma et al., 2024; Ossola et al., 2021; Peuravuori and Pihlaja, 1997). High molecular weight compounds are associated with fresh biomass-burning OA (Farley et al., 2022; Ma et al., 2024), indicating the abundance of fresh BrC. This is further corroborated by the short (1.5-3-hour) lifetime of particles during pollution events (Cesler-Maloney et al., 2024) and by source apportionment of ALPACA OA finding that fresh and lightly aged wood-burning OA on average account for 47% of the total measured OA (Ijaz et al., 2024).

3.1.3 Brown Carbon Light Absorbance

By combining the measured actinic fluxes ($I_{\lambda,AK}$), the water-soluble organic carbon concentration, and the MAC$_{\lambda}$ of DOC, we calculated the rate of light absorption by particles in Fairbanks during the peak three hours of daylight, when photochemistry is most active (Figure 4c). The peak three-hour average $R_{abs,AK,ALW}$ is 39-88% of the value at solar noon. The rate shows no notable trend across the campaign (Figure 4c): this is a result of highly variable measured actinic fluxes due to variable cloudiness, a small decrease in soluble organic aerosol concentrations from January to February, some photobleaching of BrC, and a peak in the rate of light absorption during the pollution episode. This elevated $R_{abs,AK,ALW}$ for the 1/31 composite indicates heightened potential for BrC-mediated photochemistry during the pollution episode.

3.2 Measurements of Photooxidant Production in PM Extracts

Under laboratory simulated sunlight, all particle extracts produce significant concentrations of $^{\bullet}$OH, ^{3}C*, and $^1O_2^*$. Figure 5 presents particle extract results normalized to a standard Fairbanks winter photon flux, providing insight into the capacity of water-soluble chromophores to produce photooxidants in each sample (details are in Tables S10 and S11). The average ($\pm1\sigma$) DOC concentration in PME is $2.6(\pm0.8)\times10^{-3}$ M, which is 3-4 orders of magnitude lower than aerosol liquid water but similar to DOC concentrations of cloud and fog droplets (Kaur et al., 2019; Ma et al., 2023).

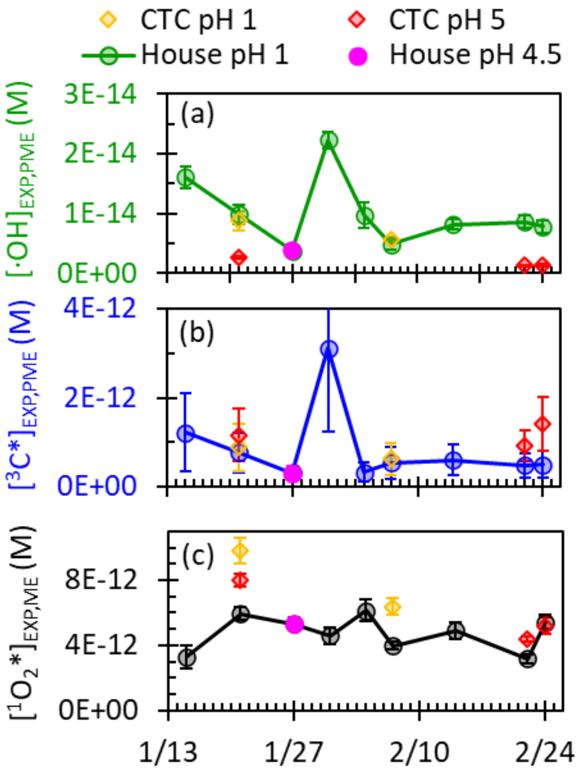

Figure 5. Steady-state concentrations of (a) $^{\bullet}$OH, (b) ^{3}C*, and (c) $^1O_2$* in particle extracts measured under laboratory simulated sunlight and normalized to actinometric conditions of $j_{2NB,AK}$ = 0.0045 s^{-1}, the Fairbanks midday photon flux modeled by TUV on February 1st, 2022. Samples were collected from two different sites (House and CTC) and were extracted at two different pH values (pH 1 and 4.5/5). The error bars represent the error propagated from each component of the calculation, including the regression to determine k'_P and the rate constants with each probe. The ^{3}C* concentrations have the highest errors mostly due to large error in the rate constant of the syringol probe with ^{3}C* at low pH.

3.2.1 Hydroxyl Radical in PM Extracts

Hydroxyl radical concentrations are variable throughout the field campaign (Figure 5a). The $^{\bullet}$OH concentration peaks during the 1/31 pollution episode at a value six times higher than the lowest value. $^{\bullet}$OH concentrations at pH 1 are moderately correlated with DOC concentration (R^2 = 0.47, p-value < 0.01) and poorly correlated with $PM_{2.5}$ concentration (R^2 = 0.28, p-value < 0.01), though both correlations are stronger than reported in past work for biomass burning samples (Figure S5) (Kaur et al., 2019; Ma et al., 2023). The correlation of $^{\bullet}$OH with DOC is unexpected: past studies have found that $^{\bullet}$OH concentrations do not increase with DOC because DOC is the dominant $^{\bullet}$OH sink (Kaur et al., 2019; Ma et al., 2023). Instead, our observed correlation suggests that DOC is either an $^{\bullet}$OH source (Gerritz et al., 2023), an $^{\bullet}$OH precursor (e.g., through HOOH formation by BrC, (Anastasio et al., 1997), or that DOC is correlated with other sources of $^{\bullet}$OH (Ma et al., 2024; Mao et al., 2013). To understand our $^{\bullet}$OH sources, we compared our measured $^{\bullet}$OH formation rates with calculated nitrate and nitrite photolysis rates based on measurement of inorganic ions, as well as the HOOH formation rate measured by Sunday et al. (2024) (Table S12). While nitrite and nitrate photolysis are negligible, the rate of HOOH formation is large enough to account for all $^{\bullet}$OH formed in our PM extracts. Furthermore, there is a strong correlation between $P_{\bullet OH,EXP,PME}$ and $P_{HOOH,EXP,PME}$ (R^2 = 0.93, p-value < 0.1; Figure S6a) and a notable correlation between $^{\bullet}$OH and water-soluble Fe (R^2 = 0.47, p-value < 0.01; Figure S6b). This suggests that photo-Fenton reactions of HOOH with metals are a major $^{\bullet}$OH source (Anastasio and McGregor, 2001; Arciva et al., 2022; Kaur et al., 2019; Ma et al., 2024; Tong et al., 2016). Further evidence can be seen in the strong pH-dependence of $^{\bullet}$OH concentrations: values at pH 5 for CTC particles are 15-30% of their pH 1 house-site counterparts, in line with the lower Fe concentrations and slower rates of HOOH production at pH 5 compared to pH 1 (Sunday et al., 2024).

3.2.2 Triplet Excited States of Brown Carbon in PM Extracts

The triplet concentrations show strong differences between clean and polluted periods (Figure 5b). ^{3}C* concentrations peak during the pollution episode and are low during clean periods when DOC concentrations are low. We observe no statistically significant pH dependence or site difference for ^{3}C*. Concentrations of ^{3}C* and $^1O_2$* are poorly correlated (R^2 = 0.04, p-

value < 0.01), a surprising observation because singlet oxygen is produced from triplets. The lack of correlation might be caused by the specificity of the syringol probe, which only quantifies the oxidizing subset of the $^3C^*$ population, while $^1O_2^*$ is produced from the total $^3C^*$ population (Bodesheim et al., 1994; Ma et al., 2022; Schweitzer et al., 2003). In general, we find that high DOC concentrations during pollution events lead to high $^3C^*$ concentrations, indicating the strong potential for triplet-driven chemistry.

3.2.3 Singlet Molecular Oxygen in PM Extracts

The $^1O_2^*$ concentrations in the House particle extracts do not change significantly across the campaign (Figure 5c). The few samples from the CTC site and at pH 5 suggest that $^1O_2^*$ generation is similar between the sites and relatively independent of acidity. Surprisingly, we found poor correlations between $^1O_2^*$ concentration and $PM_{2.5}$ ($R^2 = 0.01$, p-value < 0.01) and DOC ($R^2 = 0.11$, p-value < 0.01; Figure S5). During the 1/31 pollution episode, where $PM_{2.5}$ and DOC peaked, $^1O_2^*$ did not increase, while concentrations of $^{\bullet}OH$ and $^3C^*$ were both enhanced during the pollution event. We expected enhanced $^1O_2^*$ concentrations for the pollution event because the concentrations of BrC driving $^1O_2^*$ formation are heightened, suggesting P_{1O2^*} should increase, while the dominant $^1O_2^*$ sink in our laboratory PM extracts, water, is consistent across all extracts (Kaur et al., 2019; Ma et al., 2023). The lack of correlation between $^1O_2^*$ and DOC indicates significant variability in singlet oxygen quantum yields, as discussed below.

3.2.4 Photooxidant Quantum Yields Determined in PM Extracts

Using the photooxidant measurements, we calculated the quantum yields (Φ) of $^{\bullet}OH$, $^3C^*$, and $^1O_2^*$ in our samples (Figure 6). The average (±1σ) $\Phi_{\bullet OH}$ was 0.037(±0.018)%, similar to previously reported values in aqueous extracts of ambient $PM_{2.5}$ (Figure 6a) (Kaur et al., 2019; Ma et al., 2024). We find that $\Phi_{\bullet OH}$ is independent of sampling site but does depend on pH: the lower quantum yields at pH 5 (compared to pH 1) are likely due to the lower solubility of transition metals, which can be sources of $^{\bullet}OH$ (Sunday et al., 2025). Φ_{3C^*} was relatively stable with an average of 3.0(±1.2)%, nearly identical to the average for Davis particles (Ma et al., 2024), although our quantum yield range (1.2–4.9%) is notably narrower than in this past work (0.9–8.8%). Φ_{3C^*} demonstrates no site or pH dependence, which is likely because our MAC values and DOC concentrations show little variation with sample site or extract pH (Figure S4). In contrast to Φ_{3C^*}, the Φ_{1O2^*} of 1.8–8.5% observed in our six-week field campaign demonstrate a range of values similar to that reported in samples collected over a one-year period in Davis, CA (Ma et al., 2024). We find minor site and pH differences in Φ_{1O2^*}, but without further investigation, cannot comment on the causes. We find a significant correlation between Φ_{1O2^*} and E2/E3 ($R^2 = 0.63$, p-value < 0.01; Figure S7), even with our narrow range of E2/E3 values, which suggests that higher molecular weight DOC (which have lower E2/E3 ratios) corresponds to lower Φ_{1O2^*}. This also suggests that small changes in the average molecular weight of BrC compounds can significantly impact their ability to produce $^1O_2^*$ (Ossola et al., 2021). Altogether, we attribute the wide range of Φ_{1O2^*} values to minor differences in BrC sources or small changes in the degree of chemical aging due to reactions that might involve direct photodegradation, $^{\bullet}$OH, ^{3}C*, or ozone (Bogler et al., 2022; Leresche et al., 2021; Ma et al., 2024).

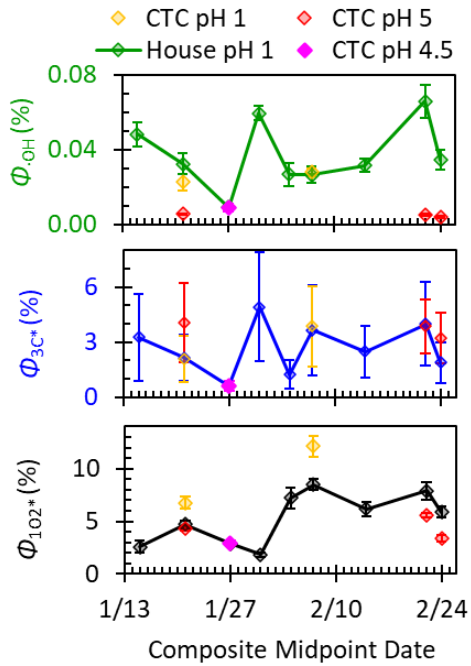

Figure 6. Quantum yields measured in dilute particle extracts under simulated sunlight laboratory conditions for (a) $^{\bullet}$OH, (b) ^{3}C*, and (c) ^{1}O$_2$*.

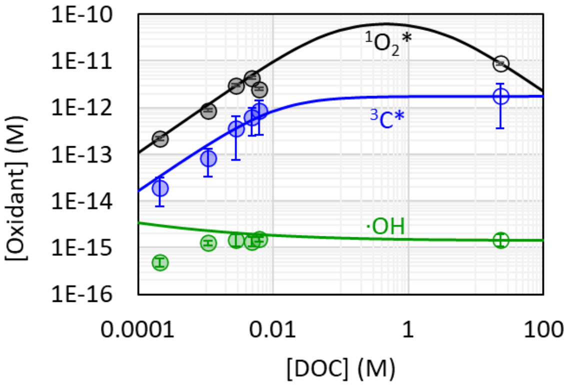

Figure 7. Kinetic models to extrapolate photooxidant concentrations from the dilution series in PM extracts to aerosol liquid water conditions for CTC sample 2/14 for singlet oxygen (gray circles), oxidizing triplets (blue circles) and hydroxyl radical (green circles). The filled circles at low DOC concentrations represent the dilution series measurements and the open circles at high DOC correspond to extrapolated values for an ALW conditions with a PM-mass/H_2O-mass ratio of 0.69 µg-PM/µg-H_2O determined for the 2/14 CTC sample. Oxidant concentrations in the dilution series and ALW extrapolation were normalized to $j_{2NB,AK}$ = 0.0045 s^{-1}, which corresponds to the average midday actinic flux for February 1st and includes the 2.5 enhancement factor due to optical confinement. Lines represent extrapolations, which were made using equations 4, 5, and 6 with parameters from Tables S14, S15, and S16. The line for $^{•}OH$ includes mass transport of $^{•}OH$ from the gas phase, which is why the green line is above the PM extract data points, which represent only aqueous sources.

3.3 Modelling Photooxidant Production in Aerosol Liquid Water

Next, we use kinetic models to predict the steady-state concentrations of $^{•}OH$, $^3C^*$, and $^1O_2^*$ in aerosol liquid water under Fairbanks actinic flux conditions using the quantum yields determined in our extracts (Figure 7). First, we used our dilution series to understand how photooxidant production changes with DOC concentration (Table S13, Figure S8). In our PM extracts, where DOC concentrations are similar to cloud/fog water conditions, $P_{•OH,EXP,PME}$, $P_{3C*,EXP,PME}$, and $P_{1O2*,EXP,PME}$ are all proportional to DOC concentration, which agrees with previous work on PM extracts from Davis, California (Kaur et al., 2019; Ma et al., 2023). To extrapolate our photooxidant concentrations to aerosol liquid water conditions, we used parameters defined by Ma et al. (2023) (Table S14) to predict how photooxidant production rates and sinks vary as a function of ALWC (Section 2.6.3), using DOC concentration as our proxy for ALW. As shown in Figure 7, concentrations of $^1O_2^*$ and $^3C^*$ are predicted to be higher in ALW compared to in PM extracts (which are roughly as concentrated as fog/cloud drops), while $^{•}OH$ is fairly stable across the entire range of DOC concentration.). Figure 8 shows the modelled photooxidant concentrations under Fairbanks actinic flux in both ALW (colored points, Table S15) and in our much more dilute PM extracts (grey points). Even in the winter in Fairbanks, we predict significant concentrations of $^{•}OH$, $^3C^*$, and $^1O_2^*$ in particles.

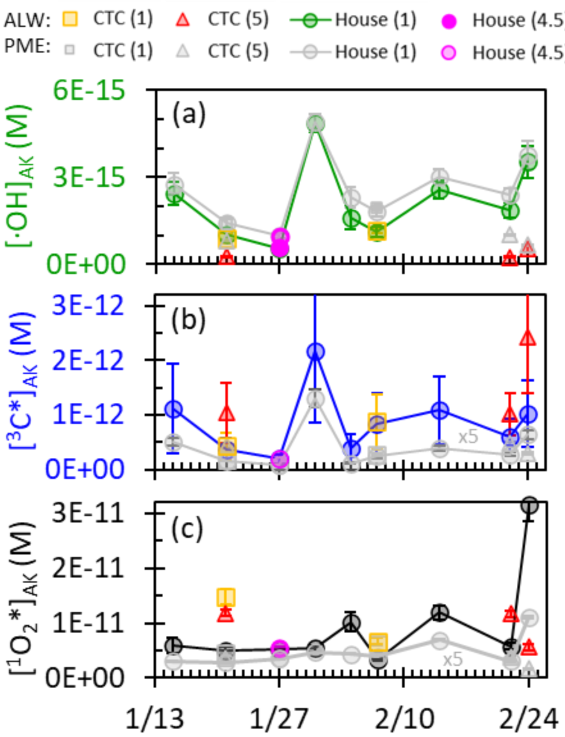

Figure 8. Predicted steady-state concentrations of (a) $^{\bullet}OH$, (b) $^3C^*$, and (c) $^1O_2^*$ under Fairbanks $I_{\lambda,AK}$ averaged over the peak three hours of sunlight for each composite period. The colored points represent concentrated ALW conditions (average [DOC] = 21(±7) M). The grey data represent results for the PM extracts (average [DOC] = $2.6(\pm0.8)\times10^{-3}$ M), i.e., Figure 5 results with added $^{\bullet}OH$ uptake form mass transport and adjusted to the measured Fairbanks $I_{\lambda,AK}$ for each composite. For (b) and (c), the PME $^3C^*$ and $^1O_2^*$ concentrations are multiplied by a factor of 5 so they can be distinguished from the x-axis. Note that CTC site samples may have a slight underestimate in DOC concentration in ALW due to using $PM_{0.7}$ samples, which may lead to a small overestimate in $^1O_2^*$ at the CTC site. The pH of each sample type is indicated in parentheses in the legend.

3.3.1 Hydroxyl Radical in ALW

Even in the winter in Fairbanks, we predict significant concentrations of $^{\bullet}OH$, $^3C^*$, and $^1O_2^*$ in particles. Midday $^{\bullet}OH$ concentrations predicted for Fairbanks ALW at pH 1 range from $(1\text{-}6)\times10^{-15}$ M (Figure 8a), similar to $^{\bullet}OH$ concentrations in ALW reported by Ma et al. (2023) in $PM_{2.5}$ from Davis, CA at midday on the winter solstice ($(6\text{-}9)\times10^{-15}$ M). The lower $^{\bullet}OH$ observed in Fairbanks is in part because of lower wintertime actinic fluxes compared to California, and in part because the Davis sunlight condition is solar noon, while the Fairbanks sunlight condition is the average peak three hours of daylight. In

ALW, we calculated the potential role two additional potential sources of $^{\bullet}$OH that would not be captured in our illumination experiments: the reactions of ozone with superoxide (Bielski et al., 1985) and ozone with phenolic moieties in DOC (Önnby et al., 2018), but each accounted for less than 1% of the measured $^{\bullet}$OH production. Of the three photooxidants discussed here, $^{\bullet}$OH is the only oxidant whose steady-state concentration does not show major differences between dilute extract conditions and concentrated aerosol liquid water conditions (Figure 8a). This is because both the production rate of $^{\bullet}$OH and its first-order rate constant for loss increase linearly with DOC concentration (as a proxy for solution concentration), as reported in past work (Kaur et al., 2019; Ma et al., 2023). For example, in our dilution experiment composite (CTC 2/14, pH 1), the predicted $P_{\bullet\mathrm{OH,ALW}}$ is roughly 8000 times higher than the measured $P_{\bullet\mathrm{OH,EXP}}$ for the standard extract, while $k'_{\bullet\mathrm{OH,ALW}}$ is also 8000 times faster than its extract value, corresponding to an $^{\bullet}$OH lifetime in ALW at pH 1 of 0.2(±0.1) nanoseconds. The minor difference in $^{\bullet}$OH concentrations between PME and ALW conditions, e.g., in Figure 7, is caused by mass transport – in dilute conditions with PM-mass/H_2O-mass ratios equal to our PM extracts, mass transport accounts for 6-50% of the $^{\bullet}$OH source, while in ALW it only accounts for 0.4-5%, leading to slightly lower $^{\bullet}$OH concentrations in ALW.

3.3.2 Triplet Excited States of Brown Carbon in ALW

We predict that Fairbanks PM also produce significant concentrations of $^3C^*$ during daylight (Figure 8b), ranging from $(0.2–2)\times10^{-12}$ M, which are at the lower end of the range of $^3C^*$ concentrations in ALW reported in California particles during winter $(0.4–13)\times10^{-12}$ M (Ma et al., 2023). Because the source of $^3C^*$ is BrC, higher DOC concentrations lead to higher $^3C^*$ production rates (Figure S8). The dominant sink for $^3C^*$ in dilute conditions is energy transfer with O_2, accounting for 90(±2)% of $^3C^*$ loss, with DOC accounting for the remaining 10(±2)% (Table S16), as seen previously (Ma et al., 2023). In ALW conditions, however, DOC concentrations are 10^3-10^4 times higher, and DOC is the dominant (> 99%) $^3C^*$ sink. Because DOC is both the dominant source and sink of $^3C^*$ in ALW, the triplet concentration plateaus at the high DOC concentrations expected in ALW (Figure 7) (Kaur et al., 2019; Ma et al., 2023). On average, predicted $^3C^*$ concentrations in ALW are 12(±4) times higher than in our extracts, similar to the enhancements reported in past work (Kaur et al., 2019; Ma et al., 2023). In ALW, the average predicted lifetime of $^3C^*$ is 0.9(±0.6) nanoseconds, almost three orders of magnitude shorter than in PM extracts (500 nanoseconds). It is worth noting that our predicted $^3C^*$ lifetimes in ALW are within the range of singlet BrC ($^1C^*$) lifetimes (0.15 – 5.5 ns) measured for humic substances in dilute surface waters. This suggests that singlet states of brown carbon might be significant for chemistry in aerosol particles.

3.3.3 Singlet Molecular Oxygen in ALW

We also predict high concentrations of $^1O_2^*$ in ALW in Fairbanks, ranging from $(4–30)\times10^{-12}$ M (Figure 8c). Surprisingly, most of our measurements fall within the range reported by Ma et al. (2023) for Davis PM ($(1–8)\times10^{-12}$ M), despite notably different wintertime photon fluxes in these two locations. We attribute this similarity to higher $\Delta P_{1\mathrm{O2*}}/\Delta\mathrm{DOC}$ values in

Fairbanks leading to comparable P_{1O2*} at both latitudes (Table S16). In addition, because the steady-state $^1O_2*$ concentration in ALW is highly dependent on the DOC concentration, similar ALW DOC concentrations in both locations leads to similar predicted $^1O_2*$ concentrations. In ALW, DOC is the dominant sink for $^1O_2*$, accounting for 88(±6)% of its loss, while in our PM extracts, DOC is a minor sink and water accounts for >99% of $^1O_2*$ loss (Table S14, Ma et al., 2023). While the rate of $^1O_2*$ loss to DOC increased at higher DOC concentrations, P_{1O2*} reaches a maximum at high DOC concentrations because P_{1O2*} is limited by the maximum $^3C*$ concentration in high DOC conditions (Figure 7). This phenomenon leads to lower $^1O_2*$ concentrations predicted at higher DOC conditions and explains why the highest $^1O_2*$ concentration was observed in the 2/24 CTC composite: warmer temperatures caused high ALW, dilute DOC concentration in ALW, and therefore slower $^1O_2*$ loss to DOC. The high $^1O_2*$ concentrations predicted here for Fairbanks PM in winter reiterates the impact of DOC on $^1O_2*$ concentrations in ALW reported by Ma et al. (2023). Overall, the high concentrations of all three photooxidants predicted for ALW suggest these oxidants are important drivers of particle-phase chemistry during winter pollution events in Fairbanks.

4 Atmospheric Implications

While measurements of $^\bullet OH$, $^3C*$, and $^1O_2*$ in ambient PM extracts indicate a strong potential role of photooxidants in heterogenous chemistry, little work has been done to assess how particle photooxidants compete against other oxidation mechanisms to contribute to $PM_{2.5}$ production and loss (Badali et al., 2015; Bogler et al., 2022; Kaur et al., 2019; Kaur and Anastasio, 2018; Leresche et al., 2021; Ma et al., 2023, 2024; Smith et al., 2014, 2015, 2016; Yu et al., 2016). Here, we first explore the lifetime of various organic species due to photooxidative loss. Next, we model secondary SO_4^{2-} formation in Fairbanks during winter pollution events, and finally we assess the potential of BrC-mediated photochemistry year-round in Fairbanks.

4.1 Effect of Photooxidants on the Lifetimes of Organic Compounds

Triplets and $^1O_2*$ are highly reactive with certain classes of organic compounds, while $^\bullet OH$ is highly reactive with nearly all classes. Using the average particle photooxidant concentrations during the peak three hours of daylight during ALPACA, we estimated the average daylight winter lifetime of several organic species (Table S17). Substituted phenols, which react rapidly with $^3C*$ and $^\bullet OH$ (Arciva et al., 2022; Ma et al., 2021), have lifetimes in Fairbanks between 3 and 6 minutes due to $^3C*$ and 9-19 hours lifetimes due to aqueous $^\bullet OH$. $^1O_2*$ also reacts appreciably with certain organic classes, such as phenols and heterocycles, leading to lifetimes of 0.4-12 hours with respect to $^1O_2*$, which is 2-74% of the lifetime due to $^\bullet OH$ for the same compounds (Manfrin et al., 2019). The lifetimes for these organic species are shorter with respect to triplets and singlet oxygen primarily because ALW concentrations of these oxidants are much higher compared to $^\bullet OH$: the average $[^3C*]:[^\bullet OH]$ and $[^1O_2*]:[^\bullet OH]$ ratios for our samples are 390 and 4200, respectively. The short lifetimes of organic compounds demonstrates that biomass-burning particles are active sites of oxidation driven by BrC photochemistry, even in winter in Fairbanks, Alaska

4.2 Secondary Sulfate Formation

In Fairbanks, traditional gas-phase S(IV) oxidants such as O_3, HOOH, and $^{\bullet}OH$ are expected to be minor sulfate sources in Fairbanks winter because of limited sunlight (Moon et al., 2024; Simpson et al., 2019). Instead, several nontraditional oxidants may be important for secondary SO_4^{2-} formation in aerosols under highly polluted conditions, including oxidation by $^3C^*$, photochemical HOOH produced inside BrC particles, HONO, and NO_2 (Anastasio et al., 1997; Sunday et al., 2025; Wang et al., 2020a, b). To assess the contribution of $^3C^*$ to secondary sulfate during ALPACA, we built a kinetic model that calculates the rates of secondary SO_4^{2-} formation by eight oxidation pathways (one gas phase and seven particle phase) during the peak three hours of daylight.

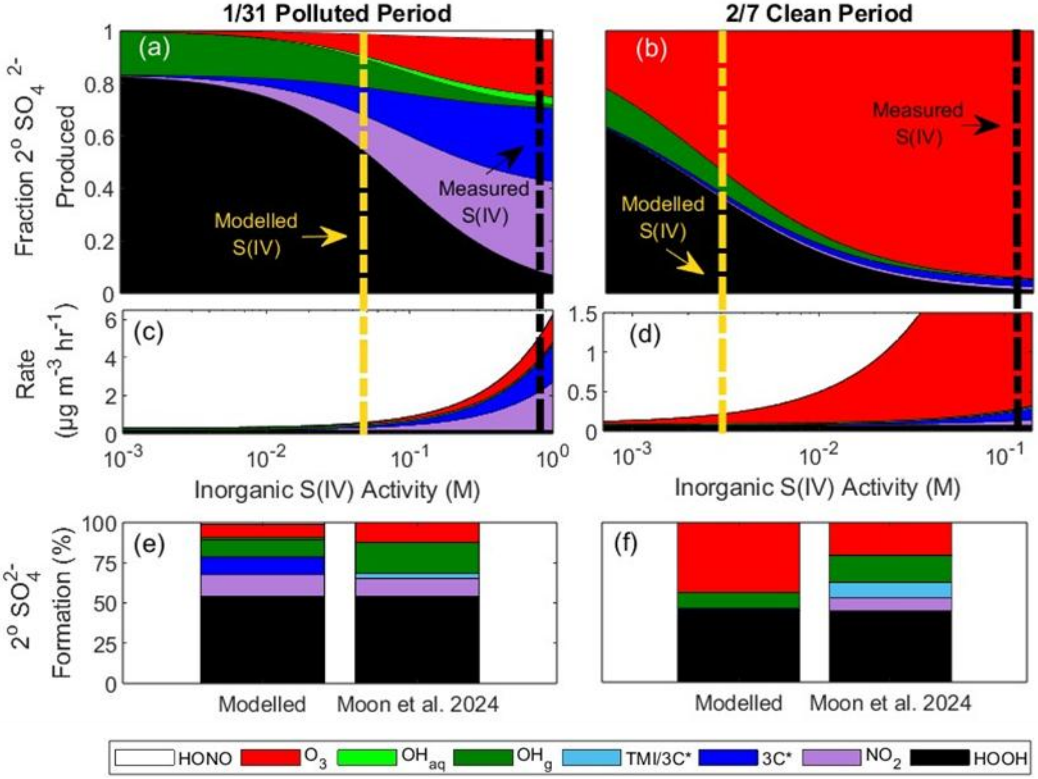

Figure 9. Modelled secondary (2°) SO_4^{2-} formation under low pH (pH 1), daytime conditions during the 1/31 polluted period and 2/7 clean period due to HOOH, NO_2, $^3C^*$, O_2 catalyzed by transition metal ions (TMI), gas-phase $^{\bullet}OH$,

aqueous-phase $^{\bullet}OH$, and O_3. Panels (a) and (b) show the fraction of secondary SO_4^{2-} formation from each oxidation pathway as a function of particle inorganic S(IV) activity. The black vertical dashed lines are the ALW inorganic S(IV) activities based on PM measurements (likely an overestimate because of contributions from organo-S(IV) compounds). The yellow vertical dashed lines are the predicted ALW inorganic S(IV) activities. Panels (c) and (d) show the total rate of secondary SO_4^{2-} formation from all pathways as a function of inorganic S(IV) activity. Panels (e) and (f) show the contribution of each oxidant to secondary SO_4^{2-} formation at the modelled activities of inorganic S(IV). Parallel results for high pH (pH 4-5) conditions are presented in Figure S9.

The kinetics for each oxidant with inorganic S(IV) (Table S18), the concentrations and activity coefficients of the oxidants (Table S19), and the activity of inorganic S(IV) (Table S20, Section S7), are summarized in the Supplementary Information. Kinetics are from the literature (Cheng et al., 2016; Ibusuki and Takeuchi, 1986; Martin and Hill, 1987; Mu et al., 2021; Seinfeld and Pandis, 2016; Song et al., 2021; Tilgner et al., 2021; Wang et al., 2020a, 2021, 2020b; Ye et al., 2021; Yu et al., 2023) while the concentrations of several key oxidants were measured and modeled during the ALPACA field campaign (Cesler-Maloney et al., 2022; Kuhn et al., 2024; Simpson et al., 2024; Sunday et al., 2025). While the rate constants and oxidant concentrations have constrained errors, the concentration of inorganic S(IV) is highly uncertain.

4.2.1 Predicting Inorganic S(IV)

The measured concentrations of inorganic S(IV) in ALPACA particles are orders of magnitude higher than expected based on Henry's law (Figure S10). Mao et al. (2024) report that up to 30% of the total particulate sulfur content was S(IV), including hydroxymethanesulfonate, other organo-S(IV) adducts, and inorganic S(IV). The measurements of inorganic S(IV) were determined in parallel extracts of the same filter with and without added HOOH to remove inorganic S(IV), but the HOOH probably also destroyed labile organo-S(IV) compounds, resulting in them also being counted as inorganic S(IV) (Campbell et al., 2022; Dingilian et al., 2024). To better constrain inorganic S(IV), we used the model to find the activity of inorganic S(IV) where the fraction of secondary SO_4^{2-} formed by HOOH in our model matched the value reported from sulfate isotope measurements by Moon et al. (2024) (Section S7). Based on this process, our modeled inorganic S(IV) activity for pH 1 particle water is, on average (±1σ), 29(±40) times lower than the "measured" inorganic S(IV) and $1.5(\pm 3.0)\times 10^{6}$ times higher than that predicted by Henry's law (Figure S10). The HOOH fraction is fixed to match the isotope results, making fractional contribution of HOOH well constrained. In contrast, the contributions from other sources are calculated only from our kinetic modeling, leaving the error in the rest of the model difficult to quantify. Nonetheless, the results provide novel insight into the contribution of competing secondary sulfate pathways, including from $^{3}C^{*}$.

4.2.2 January 31 Polluted Period

During the 1/31 polluted period, the model calculates a cumulative secondary SO_4^{2-} formation rate of 0.9 μg m^{-3} hr^{-1} at pH 1 during the peak three hours of daylight. Within the 1.5-3 hours estimated lifetime of a particle in the boundary layer during pollution episodes (Cesler-Maloney et al., 2024), this yields 1-3 μg m^{-3} of secondary SO_4^{2-}, similar to the isotope-determined measurements of 1.5 μg m^{-3} for the daytime sample collected on 1/31 (Moon et al., 2024). During the pollution episode, HOOH accounts for 54% of secondary sulfate, while NO_2, gaseous $^{\bullet}OH$, $^3C^*$, and O_3 each contribute between 8 and 14%, accounting for much of the remaining portion (Table S21). Surprisingly, local photochemistry dominates the production of secondary sulfate during ALPACA: of the modeled daytime secondary sulfate, 76% is photochemically formed by the sum of HOOH produced inside particles, gas and aqueous $^{\bullet}OH$, and particulate $^3C^*$. The sulfate isotope field measurements support the hypothesis of significant photochemical secondary SO_4^{2-}: during daylight hours on 1/31, secondary SO_4^{2-} accounted for 35% of total SO_4^{2-}, while at night, the fraction of secondary SO_4^{2-} decreased to 16% (Moon et al., 2024). Our model highlights the important, and unexpected, role of photochemistry in sulfate formation during winter pollution events in Fairbanks.

As a direct oxidant, triplets play a minor role in sulfur chemistry. The model predicts that during the 1/31 pollution episode, 10% of secondary sulfate is from $^3C^*$ during the peak three hours of daylight, while the 24-hr-average isotopic measurements attribute 3% of secondary sulfate to the $^3C^*$/TMI pathways (sulfate from $^3C^*$ and TMI are isotopically equivalent and cannot be distinguished by measurements; Section S8) (Moon et al., 2024). The difference in the measured and modeled $^3C^*$ contribution is likely because they represent different time periods: the contribution of $^3C^*$ is strongest during peak daylight and stops at sunset, leading to low 8-hour average isotopic signatures of sulfate from $^3C^*$/TMI. During peak daylight hours, we calculate 0.1 μg m^{-3} hr^{-1} of sulfate from $^3C^*$, which is 800 times slower than the 7.9 μg m^{-3} hr^{-1} upper bound predicted in past work (Wang et al., 2020b). The discrepancy stems from differences in predicted $^3C^*$ concentrations in ALW. Wang et al. (2020b) calculated triplet-mediated rates of sulfate formation using $^3C^*$ concentrations as high as 1×10^{-10} M, while recent work shows that $^3C^*$ concentrations in particles are closer to the 10^{-12} M value shown in Figure 7 (Kaur et al., 2019; Ma et al., 2023; Wang et al., 2020b). Recently, Liang et al. (2024) reported enhanced surface activity of triplets in illuminated BBOA microdroplets, leading to rapid interfacial sulfate formation, not accounted for in our model. In Fairbanks, HOOH formed from triplet-mediated reactions is more significant as an oxidant of S(IV) than are triplets themselves (Moon et al., 2024; Sunday et al., 2025).

4.2.3 February 7 Clean Period

During the 2/7 clean period, the model predicts $^3C^*$ contribute less than 1% to sulfate formation. Overall, our model has moderate agreement with the isotope measurements (Figure 9f, Table S21) (Moon et al., 2024). Because the activity of inorganic S(IV) was defined by matching the modelled and measured fraction of secondary SO_4^{2} formed by HOOH (see Section S7), both techniques agree that HOOH is the dominant formation pathway, accounting for 44% of secondary SO_4^{2-}.

The model and measurements also agree that O_3 and gas-phase $^{\bullet}OH$ are the second and third most important mechanisms, respectively. The biggest discrepancies between the model and measurements are for the $^3C^*$/TMI and NO_2 pathways: in the model these pathways each account for 1% of secondary SO_4^{2-} formation, while measurements indicate $^3C^*$/TMI and NO_2 account for 10% and 9%, respectively. The discrepancies between the model and measurements are likely because our model uses surface measurements, and therefore only represents ground-level chemistry. The well-mixed boundary layer, which is characteristic of clean periods in Fairbanks, likely transports sulfate formed aloft to the surface, which is captured in the isotopic measurements of sulfate but not by our model.

4.3 Predicted Seasonal Variations in BrC-Mediated Photochemistry

Brown-carbon-mediated photochemistry in Fairbanks is not limited to winter pollution events but could contribute to multiphase chemistry throughout the year. To investigate this, Figure 10 compares the monthly average photochemical activities of particulate BrC, gas-phase O_3 and gas-phase HONO using actinic fluxes modeled with TUV (parameters in Table S22, Finlayson-Pitts and Pitts, 2000; Seinfeld and Pandis, 2016).

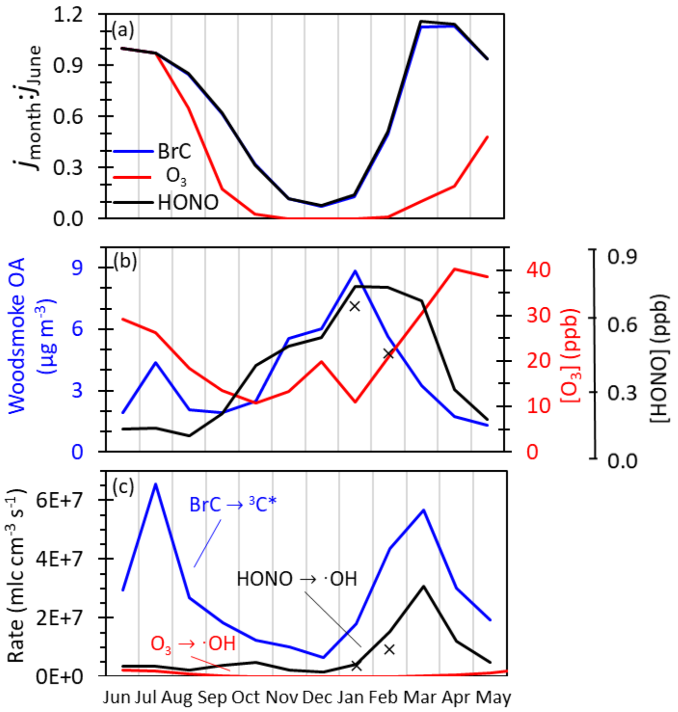

Figure 10. Predicted seasonal variations in three photochemical reactions in Fairbanks, Alaska: oxidizing triplet formation from particulate brown carbon (BrC→$^3C^*$), $^{\bullet}OH$ formation from gas-phase ozone (O_3→$^{\bullet}OH$), and $^{\bullet}OH$ formation from gas-phase nitrous acid (HONO→$^{\bullet}OH$) (Section S9). a) Photolysis rate constant (*j*) for each reaction at

solar noon on the 15th day of each month normalized to the corresponding mid-June *j* value. b) Measured or estimated monthly BBOA, O_3, and HONO concentrations (Section S10). The black line is the estimated monthly HONO and the black '×'s are monthly averaged HONO measured during ALPACA within the polluted layer (Kuhn et al., 2024). c) Predicted midday rates of each reaction on the 15th of each month. The rate of triplet formation in particles from brown carbon is expressed in equivalent gas-phase units.

Figure 10a depicts the first-order photolysis rate constants (*j*-values) for each reaction normalized to their June value (Section S9, Table S23). The photochemical production of $^{\bullet}$OH from O_3 shows a strong seasonable dependence in Fairbanks, with the January photolysis frequency only 0.2% of the June value. In contrast, brown carbon and HONO experience less seasonal dependence, with January *j*-values 13% and 14% of the June values, respectively. O_3 is more impacted by seasonal changes in the actinic flux because it absorbs shorter wavelengths of light than BrC and HONO, and short wavelengths are most suppressed during winter (Seinfeld and Pandis, 2016). Figure 10a also demonstrates the impact of albedo: long lasting snow cover leads to peak HONO and BrC *j*-values in March and April, indicating the strong potential for BrC photochemistry during this period.

Seasonal variations in the concentrations of BrC, HONO and O_3 (Figure 10b) also affect their rates of photoactivity (Section S10). The peak in woodsmoke OA and HONO concentrations during winter months enhances their dominance in winter photochemistry. In the summer, BrC photochemistry is also expected to be important because of high, yet highly variable, BrC concentrations from wildfires. HONO concentrations in Fairbanks are expected to be relatively low in summer, both because higher summertime HONO *j*-values lead to enhanced photochemical loss and because of enhanced summer vertical mixing.

Figure 10c integrates the results from panels (a) and (b) to compare the production of $^3C^*$ from BrC to the production of $^{\bullet}$OH by HONO and O_3; it clearly demonstrates that BrC-mediated photochemistry is likely important year-round. The $^3C^*$ production rate has two peaks: the first in late winter/early spring, when surface-based inversions trap copious BrC-rich wood smoke, and the second during summer, when wildfires produce abundant BrC (Kotchenruther, 2016; Robinson et al., 2024). In the cold months, triplet production in particles is on average 3.4(±0.6) times faster than gas-phase $^{\bullet}$OH production by HONO, and up to 10,000 times faster than the negligible $^{\bullet}$OH production by O_3 photolysis. Triplet production is also predicted to be rapid in the summer when wildfire smoke influences air quality. Based on the estimated $^3C^*$ formation rates during the summer of 2021, a period only moderately impacted by wildfire smoke (Figure 10c), summertime $^3C^*$ formation is much faster than $^{\bullet}$OH production: 11(±5) times faster than $^{\bullet}$OH production by HONO and 20(±10) times faster than $^{\bullet}$OH production by O_3. While oxidizing triplets are more selective than $^{\bullet}$OH, they react rapidly with multiple classes of organic compounds, including phenols (Table S17a, Arciva et al., 2022; Ma et al., 2021; Smith et al., 2014, 2015, 2016), and they are a source of HOOH (Anastasio et al., 1997; Sunday et al., 2025). Overall, Figure 10 indicates that $^3C^*$-mediated photochemistry is likely important for particle-phase chemistry year-round in Fairbanks.

5 Conclusions and Uncertainties

In this work, we characterized the production of $^\bullet OH$, $^3C^*$, and $^1O_2^*$ in aqueous particulate matter extracts collected during the winter 2022 ALPACA field campaign in Fairbanks, Alaska. We then used kinetic models to extrapolate oxidant concentrations from our dilute extracts to the concentrated conditions of aerosol liquid water. We predict significant concentrations of all three photooxidants in Fairbanks PM, at levels that are comparable to those in wintertime particles in northern California. Next, we modeled secondary sulfate formation and find that photochemistry is the dominant source of secondary sulfate during daylight hours, primarily from in-particle hydrogen peroxide, while oxidation by $^3C^*$ and aqueous $^\bullet OH$ are minor. Lastly, we estimated rates of $^3C^*$ production year-round from brown carbon in Fairbanks PM: $^3C^*$ are formed at significant rates throughout the year, with peaks during late winter pollution events and seasonal summer wildfires. Overall, this work provides insight into the unexpected role of photooxidative multiphase chemical processing of PM during winter pollution events in Fairbanks, Alaska and throughout the subarctic.

As our PM filter extracts are prepared in water, our work does not account for water-insoluble BrC. Atwi et al. (2022) report that 60% of BrC in woodsmoke PM is water-insoluble, indicating a potential missing reservoir of water-insoluble BrC capable of forming particle photooxidants. As of yet, the photochemistry driven by water-insoluble BrC has not been explored.

A significant source of uncertainty for our results is the effect of low winter temperatures on multiphase photochemistry. While we performed our experiments at 10 °C, midday temperatures in Fairbanks ranged from -33.9 to 5.2 °C during the ALPACA campaign. Temperature can impact numerous processes, including gas-particle partitioning and the rates of chemical reactions. Where thermodynamic data is available, we corrected the Henry's Law constants and reaction rate constants to Fairbanks winter temperatures (Sander, 2023; Smith et al., 2014, Table S18). However, many processes do not have a well constrained temperature dependence, including many of the quantum yields, rate constants, and absorption coefficients that we measured or used in this study. Similarly, only one of the eight sulfate formation reactions in the secondary sulfate model has a published temperature dependence. Nonetheless, our work incorporates the available temperature dependence data to provide insight into multiphase photochemistry at a high-latitude winter site.a

Another important impact of low temperature is the phase state of particles (Kiland et al., 2023; Reid et al., 2018; Shiraiwa et al., 2017; Zobrist et al., 2008). A wide body of work has demonstrated a freezing point suppression in aerosol particles. For example, Cziczo and Abbatt (1999) reported that pure water aerosols freeze only at -39 °C while supercooled ammonium sulfate (49% by weight) particles freeze at -49 °C, with higher salt concentrations leading to a larger freezing point suppression. Hearn and Smith (2005) observed rapid chemistry occurring in the organic condensed phase as low as -32 °C, while at lower temperatures the aerosol particles crystallized and chemistry stopped. We expect that particles in Fairbanks during winter are not solids but supercooled liquids, they are likely viscous (Kiland et al., 2023; Koop et al., 2011). We expect photooxidants produced in-situ will not be hindered by high viscosities: BrC is expected to continue to absorb light in viscous particles, suggesting $^3C^*$ and $^1O_2^*$ production continues in viscous conditions. We do, however, expect that the higher viscosities predicted for Fairbanks particles likely affects secondary sulfate formation because gas-phase species like SO_2 and O_3 that diffuse into the aqueous phase will be limited by slow mass transport in viscous media (Koop et al., 2011). More research is needed to constrain the impact of particle phase-state on multiphase chemistry.

The last major source of uncertainty is related to the kinetic model used to extrapolate photooxidant concentrations from bulk PM extracts to aerosol liquid water conditions. Our bulk PM extracts are roughly the concentration of cloud/fog waters, which are three-to-four orders of magnitude more dilute that aerosol liquid waters. The dilution experiment (Figure S8) constrains the relationships between photooxidant production and dissolved organic carbon content, but direct measurements of oxidant concentrations have not been made in suspended particles to confirm the extrapolation to ALW. Specific to $^1O_2^*$ in ALW, the second-order rate constant for DOC with $^1O_2^*$ – a key parameter to determine $^1O_2^*$ concentrations in particles – is not well constrained (Ma et al., 2023). Measurements are needed of photooxidant concentrations in suspended particles, and of the rate constant for $^1O_2^*$ with DOC, to fully understand multiphase photooxidant production in PM.

Data Availability.

Experimental data are available upon request. ALPACA campaign data, including actinic fluxes, are available at https://arcticdata.io/catalog/portals/ALPACA.

Author Contribution

CA, LH, WS, MS, BA, JD, JM, JHF, and JS developed the research goals and designed the experiment. AM, SK, TF, KE, MS, and BA set up the samplers in Fairbanks and collected filter samples. FG and JHF made actinic flux measurements in Fairbanks. MCM and WS made measurements of temperature, O_3, NO_2, and SO_2; JS made HONO measurements using a long-path DOAS; and JD measured particle composition at the CTC site. JC and JM modelled ALW and pH in aerosol in Fairbanks using ISORRPIA-II. LH and JH performed the photochemistry experiments. MOS and AB analyzed ions and DOC, respectively. LH analyzed the data, built the models, and prepared the manuscript with CA. Other authors provided helpful feedback on the manuscript.

Competing interests.

At least one of the (co-)authors is a member of the editorial board of Atmospheric Chemistry and Physics.

Acknowledgements

We gratefully acknowledge the following agencies for their publicly available data: the entire ALPACA team for data collection and collaboration; NOAA’s Environmental Research Division's Data Access Program (ERDDAP) website for relative humidity data (https://erddap.sensors.ioos.us/erddap/tabledap/alaska-dot-rwis-255.html, Airport Way @ Eielson Street); the Alaska Department of Environmental Conservation for year round $PM_{2.5}$, O_3, and NO_2 data; the NCAR Tropospheric Ultraviolet and Visible (TUV) Radiation Model website for actinic flux and photolysis rate constants (https://www.acom.ucar.edu/Models/TUV/Interactive_TUV/); the UC Davis Interdisciplinary Center for Plasma Mass Spectrometry (ICP-MS) for metals analysis; and Kerri Steenwerth and Kyle T. Sherbine (USDA) for ions analysis. We also thank Frank Leresche, Nadine Borduas-Dedekind, Keighan Gemmell, Claudia Sardena, and an anonymous reviewer for their comments and insights.

Financial support

This research has been supported by the National Science Foundation (Grant numbers 2109011 (UC Davis), 2109023 (UNH), 2109098 (UH), AGS-1654104 and CHE-2203419 (UC Irvine), AGS-2029747 and ICER-1927750 (UAK)), the National Oceanic and Atmospheric Administration (Grant number NA20OAR4310295 to UW), the California Agricultural Experiment Station (Project CA-D-LAW-6403-RR), and the University of California, Davis (Donald G. Crosby Graduate Fellowship in Environmental Chemistry and Jastro Shields Research Awards to L.H.).

References

Anastasio, C. and McGregor, K. G.: Chemistry of fog waters in California's Central Valley: 1. In situ photoformation of hydroxyl radical and singlet molecular oxygen, Atmos Environ, 35, 1079–1089, https://doi.org/10.1016/S1352-2310(00)00281-8, 2001.

Anastasio, C., Faust, B. C., and Rao, C. J.: Aromatic Carbonyl Compounds as Aqueous-Phase Photochemical Sources of Hydrogen Peroxide in Acidic Sulfate Aerosols, Fogs, and Clouds. 1. Non-Phenolic Methoxybenzaldehydes and Methoxyacetophenones with Reductants (Phenols), Environ Sci Technol, 31, 218–232, https://doi.org/https://doi.org/10.1021/es960359g, 1997.

Appiani, E. and McNeill, K.: Photochemical production of singlet oxygen from particulate organic matter, Environ Sci Technol, 49, 3514–3522, https://doi.org/10.1021/es505712e, 2015.

Appiani, E., Ossola, R., Latch, D. E., Erickson, P. R., and McNeill, K.: Aqueous singlet oxygen reaction kinetics of furfuryl alcohol: Effect of temperature, pH, and salt content, Environ Sci Process Impacts, 19, 507–516, https://doi.org/10.1039/c6em00646a, 2017.

Arakaki, T., Anastasio, C., Kuroki, Y., Nakajima, H., Okada, K., Kotani, Y., Handa, D., Azechi, S., Kimura, T., Tsuhako, A., and Miyagi, Y.: A General Scavenging Rate Constant for Reaction of Hydroxyl Radical with Organic Carbon in Atmospheric Waters, Environ Sci Technol, 47, 8196–8203, https://doi.org/10.1021/es401927b, 2013.

Arciva, S., Niedek, C., Mavis, C., Yoon, M., Sanchez, M. E., Zhang, Q., and Anastasio, C.: Aqueous ·OH Oxidation of Highly Substituted Phenols as a Source of Secondary Organic Aerosol, Environ Sci Technol, 56, 9959–9967, https://doi.org/10.1021/acs.est.2c02225, 2022.

Arnold, S. R., Law, K. S., Brock, C. A., Thomas, J. L., Starkweather, S. M., Von Salzen, K., Stohl, A., Sharma, S., Lund, M. T., Flanner, M. G., Petäjä, T., Tanimoto, H., Gamble, J., Dibb, J. E., Melamed, M., Johnson, N., Fidel, M., Tynkkynen, V. P., Baklanov, A., Eckhardt, S., Monks, S. A., Browse, J., and Bozem, H.: Arctic air pollution: Challenges and opportunities for the next decade, Elementa, 2016, https://doi.org/10.12952/journal.elementa.000104, 2016.

Atwi, K., Cheng, Z., El Hajj, O., Perrie, C., and Saleh, R.: A dominant contribution to light absorption by methanol-insoluble brown carbon produced in the combustion of biomass fuels typically consumed in wildland fires in the United States, Environmental Science: Atmospheres, 2, 182–191, https://doi.org/10.1039/d1ea00065a, 2022.

Badali, K. M., Zhou, S., Aljawhary, D., Antiñolo, M., Chen, W. J., Lok, A., Mungall, E., Wong, J. P. S., Zhao, R., and Abbatt, J. P. D.: Formation of hydroxyl radicals from photolysis of secondary organic aerosol material, Atmos Chem Phys, 15, 7831–7840, https://doi.org/10.5194/acp-15-7831-2015, 2015.

Bali, K., Banerji, S., Campbell, J. R., Bhakta, A. V., Chen, L. W. A., Holmes, C. D., and Mao, J.: Measurements of brown carbon and its optical properties from boreal forest fires in Alaska summer, Atmos Environ, 324, https://doi.org/10.1016/j.atmosenv.2024.120436, 2024.

Bielski, B. H., Babelli, D. E., Arudi, R. L., and Ross, A. B.: Reactivity of HO_2/O_2^- in Aqueous Solution, J. Phys. Chem. Ref. Data., 14, 1985.

Bodesheim, M., Schlitz, M., and Schmidt, R.: Triplet state energy dependence of the competitive formation of O_2 ($^1E_g^+$), O_2 ($^1\Delta_g$) and O_2 ($^3E_g^-$) in the sensitization of O_2 by triplet states, Chemical Physics Letters, 7–11 pp., 1994.

Bogler, S., Daellenbach, K. R., Bell, D. M., Prévôt, A. S. H., El Haddad, I., and Borduas-Dedekind, N.: Singlet Oxygen Seasonality in Aqueous PM_{10} is Driven by Biomass Burning and Anthropogenic Secondary Organic Aerosol, Environ Sci Technol, 56, 15389–15397, https://doi.org/10.1021/acs.est.2c04554, 2022.

Brett, N., Law, K. S., Arnold, S. R., Fochesatto, J. G., Raut, J.-C., Onishi, T., Gilliam, R., Fahey, K., Huff, D., Pouliot, G., Barret, B., Dieudonne, E., Pohorsky, R., Schmale, J., Baccarini, A., Bekki, S., Pappaccogli, G., Scoto, F., Decesari, S., Donateo, A., Cesler-Maloney, M., Simpson, W., Medina, P., D'Anna, B., Temime-Roussel, B., Savarino, J., Albertin, S., Mao, J., Alexander, B., Moon, A., DeCarlo, P. F., Selimovic, V., Yokelson, R., and Robinson, E. S.: Investigating processes influencing simulation of local Arctic wintertime anthropogenic pollution in Fairbanks, Alaska during ALPACA-2022, https://doi.org/10.5194/egusphere-2024-1450, 2024.

Campbell, J. R., Battaglia, M., Dingilian, K., Cesler-Maloney, M., St Clair, J. M., Hanisco, T. F., Robinson, E., Decarlo, P., Simpson, W., Nenes, A., Weber, R. J., and Mao, J.: Source and Chemistry of Hydroxymethanesulfonate (HMS) in Fairbanks, Alaska, Environ Sci Technol, https://doi.org/10.1021/acs.est.2c00410, 2022.

Campbell, J. R., Battaglia Jr, M., Dingilian, K. K., Cesler-Maloney, M., Simpson, W. R., Robinson, E. S., DeCarlo, P. F., Temime-Roussel, B., Holen, A. L., Wu, J., Pratt, K. A., Dibb, J. E., Nenes, A., Weber, R. J., and Mao, J.: Enhanced aqueous formation and neutralization of fine atmospheric particles driven by extreme cold, Sci. Adv, 4373 pp., 2024.

Cesler-Maloney, M., Simpson, W. R., Miles, T., Mao, J., Law, K. S., and Roberts, T. J.: Differences in Ozone and Particulate Matter Between Ground Level and 20 m Aloft are Frequent During Wintertime Surface-Based Temperature Inversions in Fairbanks, Alaska, Journal of Geophysical Research: Atmospheres, 127, https://doi.org/10.1029/2021JD036215, 2022.

Cesler-Maloney, M., Simpson, W., Kuhn, J., Stutz, J., Thomas, J., Roberts, T., Huff, D., and Cooperdock, S.: Shallow boundary layer heights controlled by the surface-based temperature inversion strength are responsible for trapping home heating emissions near the ground level in Fairbanks, Alaska, https://doi.org/10.5194/egusphere-2023-3082, 2024.

Chen, H., Ge, X., and Ye, Z.: Aqueous-Phase Secondary Organic Aerosol Formation Via Reactions with Organic Triplet Excited States—a Short Review, https://doi.org/10.1007/s40726-018-0079-7, 2018.

Cheng, Y., Zheng, G., Wei, C., Mu, Q., Zheng, B., Wang, Z., Gao, M., Zhang, Q., He, K., Carmichael, G., Pöschl, U., and Su, H.: Reactive nitrogen chemistry in aerosol water as a source of sulfate during haze events in China, Sci Adv, 2, https://doi.org/DOI: 10.1126/sciadv.1601530, 2016.

Corral Arroyo, P., David, G., Alpert, P. A., Parmentier, E. A., Ammann, M., and Signorell, R.: Amplification of light within aerosol particles accelerates in-particle photochemistry, Science (1979), 376, 293–296, https://doi.org/https://doi.org/10.1126/science.abm7915, 2022.

Crawford, J., Shetter, R. E., Lefer, B., Cantrell, C., Junkermann, W., Madronich, S., and Calvert, J.: Cloud impacts on UV spectral actinic flux observed during the International Photolysis Frequency Measurement and Model Intercomparison (IPMMI), Journal of Geophysical Research: Atmospheres, 108, https://doi.org/10.1029/2002jd002731, 2003.

Cziczo, D. J. and Abbatt, J. P. D.: Deliquescence, efflorescence, and supercooling of ammonium sulfate aerosols at low temperature: Implications for cirrus cloud formation and aerosol phase in the atmosphere, Journal of Geophysical Research Atmospheres, 104, 13781–13790, https://doi.org/10.1029/1999JD900112, 1999.

Dingilian, K., Hebert, E., Battaglia, M., Campbell, J. R., Cesler-Maloney, M., Simpson, W., St. Clair, J. M., Dibb, J., Temime-Roussel, B., D'Anna, B., Moon, A., Alexander, B., Yang, Y., Nenes, A., Mao, J., and Weber, R. J.: Hydroxymethanesulfonate and Sulfur(IV) in Fairbanks Winter During the ALPACA Study, ACS ES&T Air, 1, 646–659, https://doi.org/10.1021/acsestair.4c00012, 2024.

Edwards, K. C., Kapur, S., Fang, T., Cesler-Maloney, M., Yang, Y., Holen, A. L., Wu, J., Robinson, E. S., DeCarlo, P. F., Pratt, K. A., Weber, R. J., Simpson, W. R., and Shiraiwa, M.: Residential Wood Burning and Vehicle Emissions as Major Sources of Environmentally Persistent Free Radicals in Fairbanks, Alaska, Environ Sci Technol, https://doi.org/10.1021/acs.est.4c01206, 2024.

Farley, R., Bernays, N., Jaffe, D. A., Ketcherside, D., Hu, L., Zhou, S., Collier, S., and Zhang, Q.: Persistent Influence of Wildfire Emissions in the Western United States and Characteristics of Aged Biomass Burning Organic Aerosols under Clean Air Conditions, Environ Sci Technol, 56, 3645–3657, https://doi.org/10.1021/acs.est.1c07301, 2022.

Finlayson-Pitts, B. J. and Pitts, J. N. Jr.: Chemistry of the Upper and Lower Atmosphere: Theory, Experiments, and Applications, Academic Press, 2000.

Galbavy, E. S., Ram, K., and Anastasio, C.: 2-Nitrobenzaldehyde as a chemical actinometer for solution and ice photochemistry, J Photochem Photobiol A Chem, 209, 186–192, https://doi.org/10.1016/j.jphotochem.2009.11.013, 2010.

Gerritz, L., Schervish, M., Lakey, P. S. J., Oeij, T., Wei, J., Nizkorodov, S. A., and Shiraiwa, M.: Photoenhanced Radical Formation in Aqueous Mixtures of Levoglucosan and Benzoquinone: Implications to Photochemical Aging of Biomass-Burning Organic Aerosols, Journal of Physical Chemistry A, 127, 5209–5221, https://doi.org/10.1021/acs.jpca.3c01794, 2023.

Gerritz, L., Wei, J., Fang, T., Wong, C., Klodt, A. L., Nizkorodov, S. A., and Shiraiwa, M.: Reactive Oxygen Species Formation and Peroxide and Carbonyl Decomposition in Aqueous Photolysis of Secondary Organic Aerosols, Environ Sci Technol, 58, 4716–4726, https://doi.org/10.1021/acs.est.3c08662, 2024.

Hearn, J. D. and Smith, G. D.: Measuring rates of reaction in supercooled organic particles with implications for atmospheric aerosol, Physical Chemistry Chemical Physics, 7, 2549–2551, https://doi.org/10.1039/b506424d, 2005.

Helms, J. R., Stubbins, A., Ritchie, J. D., Minor, E. C., Kieber, D. J., and Mopper, K.: Absorption spectral slopes and slope ratios as indicators of molecular weight, source, and photobleaching of chromophoric dissolved organic matter, Limnol Oceanogr, 53, 955–969, https://doi.org/10.4319/lo.2008.53.3.0955, 2008.

Ibusuki, T. and Takeuchi, K.: Sulfur dioxide oxidation by oxygen catalyzed by mixtures of manganese(II) and iron(III) in aqueous solutions at environmental reaction conditions, Atmos Environ, 21, 1555–1560, https://doi.org/https://doi.org/10.1016/0004-6981(87)90317-9, 1986.

Ijaz, A., Temime-Roussel, B., Chazeau, B., Albertin, S., Arnold, S. R., Barrett, B., Bekki, S., Brett, N., Cesler-Maloney, M., Dieudonne, E., Dingilian, K. K., Fochesatto, J. G., Mao, J., Moon, A., Savarino, J., Simpson, W., Weber, R. J., Law, K. S., and D'Anna, B.: Complementary aerosol mass spectrometry elucidates sources of wintertime sub-micron particle pollution in Fairbanks, Alaska, during ALPACA 2022 , https://doi.org/10.5194/egusphere-2024-3789, 12 December 2024.

Jiang, W., Misovich, M. V., Hettiyadura, A. P. S., Laskin, A., McFall, A. S., Anastasio, C., and Zhang, Q.: Photosensitized Reactions of a Phenolic Carbonyl from Wood Combustion in the Aqueous Phase - Chemical Evolution and Light Absorption Properties of AqSOA, Environ Sci Technol, 55, 5199–5211, https://doi.org/10.1021/acs.est.0c07581, 2021.

Jiang, W., Ma, L., Niedek, C., Anastasio, C., and Zhang, Q.: Chemical and Light-Absorption Properties of Water-Soluble Organic Aerosols in Northern California and Photooxidant Production by Brown Carbon Components, ACS Earth Space Chem, 7, 1107–1119, https://doi.org/10.1021/acsearthspacechem.3c00022, 2023a.

Jiang, W., Niedek, C., Anastasio, C., and Zhang, Q.: Photoaging of phenolic secondary organic aerosol in the aqueous phase: evolution of chemical and optical properties and effects of oxidants, Atmos Chem Phys, 23, 7103–7120, https://doi.org/10.5194/acp-23-7103-2023, 2023b.

Joo, T., Machesky, J. E., Zeng, L., Hass-Mitchell, T., Weber, R. J., Gentner, D. R., and Ng, N. L.: Secondary Brown Carbon Formation From Photooxidation of Furans From Biomass Burning, Geophys Res Lett, 51, https://doi.org/10.1029/2023GL104900, 2024.

Kapur, S., Edwards, K. C., Fang, T., Schervish, M., Lakey, P. S. J., Yang, Y., Robinson, E. S., DeCarlo, P. F., Simpson, W. R., Weber, R. J., and Shiraiwa, M.: Reactive oxygen species, environmentally persistent free radicals, and oxidative potential of outdoor and indoor particulate matter in Wintertime Fairbanks, Alaska, Aerosol Science and Technology, https://doi.org/10.1080/02786826.2024.2433656, 2024.

Kaur, R. and Anastasio, C.: First Measurements of Organic Triplet Excited States in Atmospheric Waters, Environ Sci Technol, 52, 5218–5226, https://doi.org/10.1021/acs.est.7b06699, 2018.

Kaur, R., Labins, J. R., Helbock, S. S., Jiang, W., Bein, K. J., Zhang, Q., and Anastasio, C.: Photooxidants from brown carbon and other chromophores in illuminated particle extracts, Atmos Chem Phys, 19, 6579–6594, https://doi.org/10.5194/acp-19-6579-2019, 2019.

Kiland, K. J., Mahrt, F., Peng, L., Nikkho, S., Zaks, J., Crescenzo, G. V., and Bertram, A. K.: Viscosity, Glass Formation, and Mixing Times within Secondary Organic Aerosol from Biomass Burning Phenolics, ACS Earth Space Chem, 7, 1388–1400, https://doi.org/10.1021/acsearthspacechem.3c00039, 2023.

Koop, T., Bookhold, J., Shiraiwa, M., and Pöschl, U.: Glass transition and phase state of organic compounds: Dependency on molecular properties and implications for secondary organic aerosols in the atmosphere, Physical Chemistry Chemical Physics, 13, 19238–19255, https://doi.org/10.1039/c1cp22617g, 2011.

Kotchenruther, R. A.: Source apportionment of PM2.5 at multiple Northwest U.S. sites: Assessing regional winter wood smoke impacts from residential wood combustion, Atmos Environ, 142, 210–219, https://doi.org/10.1016/j.atmosenv.2016.07.048, 2016.

Kuhn, J., Stutz, J., Bartels-Rausch, T., Thomas, J. L., Cesler-Maloney, M., Simpson, W., Dibb, J. E., Heinlein, L. M. D., and Anastasio, C.: The interplay between snow and polluted air masses in cold urban environments, Faraday Discuss, https://doi.org/10.1039/D4FD00176A, 2024.

Laskin, A., Laskin, J., and Nizkorodov, S. A.: Chemistry of Atmospheric Brown Carbon, Chem Rev, 115, 4335–4382, https://doi.org/10.1021/cr5006167, 2015.

Laskin, A., West, C. P., and Hettiyadura, A. P. S.: Molecular insights into the composition, sources, and aging of atmospheric brown carbon, Chem Soc Rev, 54, 1583–1612, https://doi.org/10.1039/D3CS00609C, 2025.

Leresche, F., Salazar, J. R., Pfotenhauer, D. J., Hannigan, M. P., Majestic, B. J., and Rosario-Ortiz, F. L.: Photochemical Aging of Atmospheric Particulate Matter in the Aqueous Phase, Environ Sci Technol, 55, 13152–13163, https://doi.org/10.1021/acs.est.1c00978, 2021.

Li, J., Zhang, Q., Wang, G., Li, J., Wu, C., Liu, L., Wang, J., Jiang, W., Li, L., Fai Ho, K., and Cao, J.: Optical properties and molecular compositions of water-soluble and water-insoluble brown carbon (BrC) aerosols in northwest China, Atmos Chem Phys, 20, 4889–4904, https://doi.org/10.5194/acp-20-4889-2020, 2020.

Liang, Z., Zhou, L., Chang, Y., Qin, Y., and Chan, C. K.: Biomass-burning organic aerosols as a pool of atmospheric reactive triplets to drive multiphase sulfate formation, Proc Natl Acad Sci U S A, 121, https://doi.org/10.1073/pnas.2416803121, 2024.

Lyu, Y., Lam, Y. H., Li, Y., Borduas-Dedekind, N., and Nah, T.: Seasonal variations in the production of singlet oxygen and organic triplet excited states in aqueous $PM_{2.5}$ in Hong Kong SAR, South China, Atmos Chem Phys, 23, 9245–9263, https://doi.org/10.5194/acp-23-9245-2023, 2023.

Ma, L., Guzman, C., Niedek, C., Tran, T., Zhang, Q., and Anastasio, C.: Kinetics and Mass Yields of Aqueous Secondary Organic Aerosol from Highly Substituted Phenols Reacting with a Triplet Excited State, Environ Sci Technol, 55, 5772–5781, https://doi.org/10.1021/acs.est.1c00575, 2021.

Ma, L., Worland, R., Tran, T., and Anastasio, C.: Evaluation of Probes to Measure Oxidizing Organic Triplet Excited States in Aerosol Liquid Water, Environ Sci Technol, 57, 6052–6062, https://doi.org/10.1021/acs.est.2c09672, 2022.

Ma, L., Worland, R., Jiang, W., Niedek, C., Guzman, C., Bein, K. J., Zhang, Q., and Anastasio, C.: Predicting photooxidant concentrations in aerosol liquid water based on laboratory extracts of ambient particles, Atmos Chem Phys, 23, 8805–8821, https://doi.org/10.5194/acp-23-8805-2023, 2023.

Ma, L., Worland, R., Heinlein, L., Guzman, C., Jiang, W., Niedek, C., Bein, K. J., Zhang, Q., and Anastasio, C.: Seasonal variations in photooxidant formation and light absorption in aqueous extracts of ambient particles, Atmos Chem Phys, 24, 1–21, https://doi.org/10.5194/acp-24-1-2024, 2024.

Madronich, S. and Flocke, S.: The role of solar radiation in atmospheric chemistry, in: Handbook of Environmental Chemistry, Springer-Verlag, 1–26, 1998.

Manfrin, A., Nizkorodov, S. A., Malecha, K. T., Getzinger, G. J., McNeill, K., and Borduas-Dedekind, N.: Reactive Oxygen Species Production from Secondary Organic Aerosols: The Importance of Singlet Oxygen, Environ Sci Technol, 53, 8553–8562, https://doi.org/10.1021/acs.est.9b01609, 2019.

Mao, J., Fan, S., Jacob, D. J., and Travis, K. R.: Radical loss in the atmosphere from Cu-Fe redox coupling in aerosols, Atmos Chem Phys, 13, 509–519, https://doi.org/10.5194/acp-13-509-2013, 2013.

Mao, J., Bali, K., Campbell, J. R., Robinson, E. S., DeCarlo, P. F., Ijaz, A., Temime-Roussel, B., Barbara, D., Ketcherside, D., Yokelson, R. J., Hu, L., Cesler-Maloney, M., Simpson, W., Guo, F., Flynn, J., St. Clair, J., Nenes, A., and Weber, R.: Multiphase sulfur chemistry facilitates particle growth in a cold and dark urban environment, Faraday Discuss, https://doi.org/10.1039/D4FD00170B, 2024.

Martin, L. R. and Hill, M. W.: The Effect of Ionic Strength on the Manganese Catalyzed Oxidation of Sulfur (IV), Atmos Environ, 21, 2267–2270, https://doi.org/https://doi.org/10.1016/0004-6981(87)90361-1, 1987.

McNeill, K. and Canonica, S.: Triplet state dissolved organic matter in aquatic photochemistry: Reaction mechanisms, substrate scope, and photophysical properties, Environ Sci Process Impacts, 18, 1381–1399, https://doi.org/10.1039/c6em00408c, 2016.

Moon, A., Jongebloed, U., Dingilian, K. K., Schauer, A. J., Chan, Y.-C., Cesler-Maloney, M., Simpson, W. R., Weber, R. J., Tsiang, L., Yazbeck, F., Zhai, S., Wedum, A., Turner, A. J., Albertin, S., Bekki, S., Savarino, J., Gribanov, K., Pratt, K. A., Costa, E. J., Anastasio, C., Sunday, M. O., Heinlein, L. M. D., Mao, J., and Alexander, B.: Primary Sulfate Is the Dominant Source of Particulate Sulfate during Winter in Fairbanks, Alaska, ES&T Air, 1, 139–149, https://doi.org/10.1021/acsestair.3c00023, 2024.

Mu, Y., Chen, J., Herrmann, H., Ye, C., Chen, H., Hoffmann, E. H., Mettke, P., Tilgner, A., He, L., Mutzel, A., Brüggemann, M., Poulain, L., Schaefer, T., Heinold, B., Ma, Z., Liu, P., Xue, C., Zhao, X., Zhang, C., Zhang, F., Sun, H., Li, Q., Wang, L., Yang, X., Wang, J., Liu, C., and Xing, C.: Particle-phase photoreactions of Hulis and TMIs establish a strong source of H_2O_2 and particulate sulfate in the winter North China Plain, Environ Sci Technol, 55, 7818–7830, https://doi.org/10.1021/acs.est.1c00561, 2021.

Önnby, L., Salhi, E., McKay, G., Rosario-Ortiz, F. L., and von Gunten, U.: Ozone and chlorine reactions with dissolved organic matter - Assessment of oxidant-reactive moieties by optical measurements and the electron donating capacities, Water Res, 144, 64–75, https://doi.org/10.1016/j.watres.2018.06.059, 2018.

Ossola, R., Jönsson, O. M., Moor, K., and McNeill, K.: Singlet Oxygen Quantum Yields in Environmental Waters, Chem Rev, 121, 4100–4146, https://doi.org/10.1021/acs.chemrev.0c00781, 2021.

Peuravuori, J. and Pihlaja, K.: Molecular size distribution and spectroscopic properties of aquatic humic substances, Anal Chim Acta, 337, 133–149, 1997.

Reid, J. P., Bertram, A. K., Topping, D. O., Laskin, A., Martin, S. T., Petters, M. D., Pope, F. D., and Rovelli, G.: The viscosity of atmospherically relevant organic particles, https://doi.org/10.1038/s41467-018-03027-z, 2018.

Remke, S. C., Bürgin, T. H., Ludvíková, L., Heger, D., Wenger, O. S., von Gunten, U., and Canonica, S.: Photochemical oxidation of phenols and anilines mediated by phenoxyl radicals in aqueous solution, Water Res, 213, https://doi.org/10.1016/j.watres.2022.118095, 2022.

Robinson, E. S., Cesler-Maloney, M., Tan, X., Mao, J., Simpson, W., and DeCarlo, P. F.: Wintertime spatial patterns of particulate matter in Fairbanks, AK during ALPACA 2022, Environmental Science: Atmospheres, 3, 568–580, https://doi.org/10.1039/d2ea00140c, 2023.

Robinson, E. S., Battaglia, M., Campbell, J. R., Cesler-Maloney, M., Simpson, W., Mao, J., Weber, R. J., and DeCarlo, P. F.: Multi-year, high-time resolution aerosol chemical composition and mass measurements from Fairbanks, Alaska, Environmental Science: Atmospheres, 4, 685–698, https://doi.org/10.1039/d4ea00008k, 2024.

Sander, R.: Compilation of Henry’s law constants (version 5.0.0) for water as solvent, https://doi.org/10.5194/acp-23-10901-2023, 6 October 2023.

Schmale, J., Arnold, S. R., Law, K. S., Thorp, T., Anenberg, S., Simpson, W. R., Mao, J., and Pratt, K. A.: Local Arctic Air Pollution: A Neglected but Serious Problem, Earths Future, 6, 1385–1412, https://doi.org/10.1029/2018EF000952, 2018.

Schweitzer, G., Gronheid, R., Jordens, S., Lor, M., De Belder, G., Weil, T., Reuther, E., Müllen, K., and De Schryver, F. C.: Intramolecular directional energy transfer processes in dendrimers containing perylene and terrylene chromophores, Journal of Physical Chemistry A, 107, 3199–3207, https://doi.org/10.1021/jp026459s, 2003.

Seinfeld, J. H. and Pandis, S. N.: Atmospheric Chemistry and Physics: From Air Pollution to Climate Change, 3rd ed., Wiley, 2016.

Shiraiwa, M., Li, Y., Tsimpidi, A. P., Karydis, V. A., Berkemeier, T., Pandis, S. N., Lelieveld, J., Koop, T., and Pöschl, U.: Global distribution of particle phase state in atmospheric secondary organic aerosols, Nat Commun, 8, https://doi.org/10.1038/ncomms15002, 2017.

Simpson, W., Law, K., Schmale, J., Pratt, K., Arnold, S., Mao, J., Alexander, B., Anenberg, S., Baklanov, A., Bell, D., Brown, S., Creamean, J., de Boer, G., DeCarlo, P., Descari, S., Elleman, R., Flynn, J., Fochesatto, J., Ganzenfeld, L., Griffin, R., Järvi, L., Kaspari, S., Konstantinov, P., Murphy, J., Petäjä, T., Pye, H., Jean-Christophe Raut, J.-C., Roberts, T., Shiraiwa, M., Stutz, J., Thomas, J., Thornton, J., Weber, R., Webley, P., and Williams, B.: Alaskan Layered Pollution And Chemical Analysis (ALPACA) White Paper, 2019.

Simpson, W. R., Mao, J., Fochesatto, G. J., Law, K. S., DeCarlo, P. F., Schmale, J., Pratt, K. A., Arnold, S. R., Stutz, J., Dibb, J. E., Creamean, J. M., Weber, R. J., Williams, B. J., Alexander, B., Hu, L., Yokelson, R. J., Shiraiwa, M., Decesari, S., Anastasio, C., D’Anna, B., Gilliam, R. C., Nenes, A., St. Clair, J. M., Trost, B., Flynn, J. H., Savarino, J., Conner, L. D., Kettle, N., Heeringa, K. M., Albertin, S., Baccarini, A., Barret, B., Battaglia, M. A., Bekki, S., Brado, T. J., Brett, N., Brus, D., Campbell, J. R., Cesler-Maloney, M., Cooperdock, S., Cysneiros de Carvalho, K., Delbarre, H., DeMott, P. J., Dennehy, C. J. S., Dieudonné, E., Dingilian, K. K., Donateo, A., Doulgeris, K. M., Edwards, K. C., Fahey, K., Fang, T., Guo, F., Heinlein, L. M. D., Holen, A. L., Huff, D., Ijaz, A., Johnson, S., Kapur, S., Ketcherside, D. T., Levin, E., Lill, E., Moon, A. R., Onishi, T., Pappaccogli, G., Perkins, R., Pohorsky, R., Raut, J.-C., Ravetta, F., Roberts, T., Robinson, E. S., Scoto, F., Selimovic, V., Sunday, M. O., Temime-Roussel, B., Tian, X., Wu, J., and Yang, Y.: Overview of the Alaskan Layered Pollution and Chemical Analysis (ALPACA) Field Experiment, ACS ES&T Air, 1, 200–222, https://doi.org/10.1021/acsestair.3c00076, 2024.

Smith, J. D., Sio, V., Yu, L., Zhang, Q., and Anastasio, C.: Secondary organic aerosol production from aqueous reactions of atmospheric phenols with an organic triplet excited state, Environ Sci Technol, 48, 1049–1057, https://doi.org/10.1021/es4045715, 2014.

Smith, J. D., Kinney, H., and Anastasio, C.: Aqueous benzene-diols react with an organic triplet excited state and hydroxyl radical to form secondary organic aerosol, Physical Chemistry Chemical Physics, 17, 10227–10237, https://doi.org/10.1039/c4cp06095d, 2015.

Smith, J. D., Kinney, H., and Anastasio, C.: Phenolic carbonyls undergo rapid aqueous photodegradation to form low-volatility, light-absorbing products, Atmos Environ, 126, 36–44, https://doi.org/10.1016/j.atmosenv.2015.11.035, 2016.

Song, H., Lu, K., Ye, C., Dong, H., Li, S., Chen, S., Wu, Z., Zheng, M., Zeng, L., Hu, M., and Zhang, Y.: A comprehensive observation-based multiphase chemical model analysis of sulfur dioxide oxidations in both summer and winter, Atmos Chem Phys, 21, 13713–13727, https://doi.org/10.5194/acp-21-13713-2021, 2021.

Sunday, M. O., Heinlein, L. M. D., He, J., Moon, A., Kapur, S., Fang, T., Edwards, K. C., Guo, F., Dibb, J., Flynn III, J. H., Alexander, B., Shiraiwa, M., and Anastasio, C.: Hydrogen Peroxide Photoformation in Particulate Matter and its Contribution to S(IV) Oxidation During Winter in Fairbanks, Alaska, Atmos Chem Phys, 25, 5087–5100, https://doi.org/10.5194/acp-25-5087-2025, 2025.

Tilgner, A., Schaefer, T., Alexander, B., Barth, M., Collett, J. L., Fahey, K. M., Nenes, A., Pye, H. O. T., Herrmann, H., and McNeill, V. F.: Acidity and the multiphase chemistry of atmospheric aqueous particles and clouds, Atmos Chem Phys, 21, 13483–13536, https://doi.org/10.5194/acp-21-13483-2021, 2021.

Tomaz, S., Cui, T., Chen, Y., Sexton, K. G., Roberts, J. M., Warneke, C., Yokelson, R. J., Surratt, J. D., and Turpin, B. J.: Photochemical Cloud Processing of Primary Wildfire Emissions as a Potential Source of Secondary Organic Aerosol, Environ Sci Technol, 52, 11027–11037, https://doi.org/10.1021/acs.est.8b03293, 2018.

Tong, H., Arangio, A. M., Lakey, P. S. J., Berkemeier, T., Liu, F., Kampf, C. J., Brune, W. H., Poschl, U., and Shiraiwa, M.: Hydroxyl radicals from secondary organic aerosol decomposition in water, Atmos Chem Phys, 16, 1761–1771, https://doi.org/10.5194/acp-16-1761-2016, 2016.

Virtanen, A., Joutsensaari, J., Koop, T., Kannosto, J., Yli-Pirilä, P., Leskinen, J., Mäkelä, J. M., Holopainen, J. K., Pöschl, U., Kulmala, M., Worsnop, D. R., and Laaksonen, A.: An amorphous solid state of biogenic secondary organic aerosol particles, Nature, 467, 824–827, https://doi.org/10.1038/nature09455, 2010.

Wang, J., Li, J., Ye, J., Zhao, J., Wu, Y., Hu, J., Liu, D., Nie, D., Shen, F., Huang, X., Huang, D. D., Ji, D., Sun, X., Xu, W., Guo, J., Song, S., Qin, Y., Liu, P., Turner, J. R., Lee, H. C., Hwang, S., Liao, H., Martin, S. T., Zhang, Q., Chen, M., Sun, Y., Ge, X., and Jacob, D. J.: Fast sulfate formation from oxidation of SO_2 by NO_2 and HONO observed in Beijing haze, Nat Commun, 11, https://doi.org/10.1038/s41467-020-16683-x, 2020a.

Wang, W., Liu, M., Wang, T., Song, Y., Zhou, L., Cao, J., Hu, J., Tang, G., Chen, Z., Li, Z., Xu, Z., Peng, C., Lian, C., Chen, Y., Pan, Y., Zhang, Y., Sun, Y., Li, W., Zhu, T., Tian, H., and Ge, M.: Sulfate formation is dominated by manganese-catalyzed oxidation of SO2 on aerosol surfaces during haze events, Nat Commun, 12, https://doi.org/10.1038/s41467-021-22091-6, 2021.

Wang, X., Gemayel, R., Hayeck, N., Perrier, S., Charbonnel, N., Xu, C., Chen, H., Zhu, C., Zhang, L., Wang, L., Nizkorodov, S. A., Wang, X., Wang, Z., Wang, T., Mellouki, A., Riva, M., Chen, J., and George, C.: Atmospheric Photosensitization: A New Pathway for Sulfate Formation, Environ Sci Technol, 54, 3114–3120, https://doi.org/10.1021/acs.est.9b06347, 2020b.

Xie, M., Hays, M. D., and Holder, A. L.: Light-Absorbing organic carbon from prescribed and laboratory biomass burning and gasoline vehicle emissions, Sci Rep, 7, https://doi.org/10.1038/s41598-017-06981-8, 2017.

Ye, C., Mu, Y., Chen, J., Chen, H., Hoffmann, E. H., Mettke, P., Tilgner, A., He, L., Mutzel, A., Brüggemann, M., Herrmann, H., Poulain, L., Schaefer, T., Heinold, B., Ma, Z., Liu, P., Xue, C., Zhao, X., Zhang, C., Zhang, F., Sun, H., Li, Q., Wang, L., Yang, X., Wang, J., Liu, C., and Xing, C.: Particle-phase photoreactions of HULIS and TMIs establish a strong source of H_2O_2 and particulate sulfate in the winter North China Plain, Environ Sci Technol, 55, 7818–7830, https://doi.org/10.1021/acs.est.1c00561, 2021.

Yu, C., Liu, T., Ge, D., Nie, W., Chi, X., and Ding, A.: Ionic Strength Enhances the Multiphase Oxidation Rate of Sulfur Dioxide by Ozone in Aqueous Aerosols: Implications for Sulfate Production in the Marine Atmosphere, Environ Sci Technol, 57, 6609–6615, https://doi.org/10.1021/acs.est.3c00212, 2023.

Yu, L., Smith, J., Laskin, A., Anastasio, C., Laskin, J., and Zhang, Q.: Chemical characterization of SOA formed from aqueous-phase reactions of phenols with the triplet excited state of carbonyl and hydroxyl radical, Atmos Chem Phys, 14, 13801–13816, https://doi.org/10.5194/acp-14-13801-2014, 2014.

Yu, L., Smith, J., Laskin, A., M George, K., Anastasio, C., Laskin, J., M Dillner, A., and Zhang, Q.: Molecular transformations of phenolic SOA during photochemical aging in the aqueous phase: Competition among oligomerization, functionalization, and fragmentation, Atmos Chem Phys, 16, 4511–4527, https://doi.org/10.5194/acp-16-4511-2016, 2016.

Zhang, J., Shrivastava, M., Zelenyuk, A., Zaveri, R. A., Surratt, J. D., Riva, M., Bell, D., and Glasius, M.: Observationally Constrained Modeling of the Reactive Uptake of Isoprene-Derived Epoxydiols under Elevated Relative Humidity and

Varying Acidity of Seed Aerosol Conditions, ACS Earth Space Chem, https://doi.org/10.1021/acsearthspacechem.2c00358, 2022.

Zobrist, B., Marcolli, C., Pedernera, D. A., and Koop, T.: Do atmospheric aerosols form glasses?, Atmos. Chem. Phys, 5221–5244 pp., 2008.